UNIVERSITY OF READING

DEPARTMENT OF METEOROLOGY

Modelling the diurnal cycle of shallow convection over land with the new Met Office NERC Cloud model

---

Author:
Emer B. Flood

Supervisors:
Dr. Chimene Daleu
Dr. Natalie Harvey
Prof. Robert Plant

A dissertation submitted in partial fulfilment of the requirement for the degree of Master of Science in Atmosphere, Ocean and Climate.

August 2019

UNIVERSITY OF READING

Abstract

The diurnal cycle of shallow convection over land is studied. An in-depth knowledge of the life cycle of shallow convection is required for the improvement of currently under-preforming parameterisation schemes used in general circulation and forecast models. The new Met Office NERC Cloud model is a cloud resolving model used to simulate a diurnal cycle of convection as observed at the Atmospheric Radiation Measurement facility located in the Southern Great Plains in the United States. The output from the Met Office NERC Cloud model is in agreement with results from other cloud resolving models. Simulations are run to investigate the factors that control the diurnal cycle of shallow convection, namely initial domain-mean thermodynamic conditions and initial thermodynamic variability. Initial thermodynamic variability is found to have the weakest influence on the diurnal cycle. Thermodynamic fluctuations resulting from a previous diurnal cycle act to bring forward the development of clouds by one hour. However, the amount of cloud produced and cloud depth are not affected, whilst turbulent motions and horizontal and vertical velocity variance are enhanced. The initial humidity profile of the atmosphere is found to have a significant impact on shallow convection. The time of cloud production, and the amount of cloud produced is dependent on the initial humidity. Higher initial moisture levels results in an increased rate of convective development, producing deeper clouds, and increasing the moisture transport from boundary layer to free troposphere. An initially drier atmosphere however will suppress this transport of mass and moisture into the free troposphere, and enhance boundary layer convection. The initial atmospheric stability has similar control as that of initial humidity. The initial stability of the free troposphere and the stability of the boundary layer are found to have different impacts on the development of shallow convection. The free tropospheric stability influences the development of clouds significantly. A reduction of free tropospheric stability has a similar effect as an increase in initial humidity. Convection is deepened, resulting in higher cloud-tops, and cloud fraction. Unlike initial humidity however, the free tropospheric stability does not affect the time of cloud initiation. The time of cloud formation is instead dependent on initial boundary layer stability and moisture content. Boundary layer stability influences the initial development of clouds and does not have any control on the development of clouds in their mature stage of development.

Contents

List of Figures

1 Introduction

1.1 Background

Shallow convection is an integral part of atmospheric dynamics on a large range of spatial and temporal scales – from organised local convection to large scale global circulations. The abundance of boundary layer cloud and its proximity to the earth's surface result in strong radiative feedbacks, contributing significantly to the earth's energy budget. For accurate weather forecasting and climate simulations, shallow convection requires proper representation within numerical models. This proves to be a difficult task, as it involves the parameterisation of numerous processes such as boundary layer diffusion, cloud condensation and radiative effects, all of which interact with each other. This section will describe the relevance of shallow convection to our climate system, show the need for a thorough understanding of its life cycles, as well as an introduction to some of the approaches taken regarding the modelling of shallow convection.

1.1.1 Shallow Convection

Shallow convection refers to moist or dry atmospheric circulation within the boundary layer that is driven by surface heating and leads to a well-mixed layer. The term boundary layer refers to the layer of well-mixed, turbulent atmosphere on the earth's surface that is capped with a temperature inversion. Shallow convection influences the depth of the boundary layer as motion produces turbulent eddies which enhance vertical mixing. Shallow convection is ubiquitous across the globe, particularly in the subtropics and trade wind regions. Cumulus and stratocumulus clouds can form at the top of the boundary layer during moist shallow convection. Shallow convective cloud can also be defined as cloud forming in the lower troposphere with a depth in pressure of less than 200hPa or a depth in height of less than 2km-3km. The term "subcloud layer" describes the portion of the boundary layer that extends from the surface up to cloud-base. Unlike deep convection, large scale low-level convergence is not necessary for its production, and can occur just as a result of boundary layer turbulence.

Shallow convection can occur over both land and sea, although the magnitude of surface forcing and the strength of the diurnal cycle is significantly stronger over land. Diurnal convection is an important mode of variability as it is responsible for daily precipitation cycles. Models show that globally 60% of precipitation results from moist convection, and in the tropics moist convection accounts for 75% of precipitation (Plant and Yano, 2016). A significant amount of this precipitation can be attributed to shallow convection, as shallow convection contributes to a number of dynamics within the atmosphere, and to the climate system. It is a vital component in the earth's radiation and hydrological budgets, it controls the transition into deep convection, and influences large scale tropical circulations. Because of these crucial roles in the atmospheric energy system, shallow convection is integral to weather forecasting and is also of great interest with regards a warming climate in the future.

Shallow convection plays an important role in the radiation processes that take part in the earth's atmosphere. Main cloud radiative interactions include the reflection of incoming radiation due to albedo, the absorption of radiation and the re-emission of outgoing long-wave radiation (OLR). Such interactions result in cloud-radiation feedbacks. For example, shallow cumulus increases radiative forcing and therefore temperature, which results in a negative feedback due a higher cloud liquid water content and the enhancement of albedo (Rieck et al., 2012). The presence and quantity of clouds in the atmosphere influences the amount of radiation or energy that is incident on the earth's surface. Different cloud types are associated with certain radiative processes more than others. The effect of cloud type on radiative processes in the atmosphere was investigated in a study by Hartmann et al. (1992). By relating radiation values to cloud type, it was found that low cloud dominates the total cloud contribution to the earth's energy balance. In their abundance, low lying boundary layer clouds reduce incoming radiation to earth's surface because of their albedo. Although high, thick clouds also reflect a significant amount of radiation, they emit OLR which counterbalances their albedo effect. Low lying clouds account for 60% of net cloud forcing (Hartmann et al., 1992).

It is well established from studies that shallow convection acts as a gate for moisture from the surface into the troposphere (Salathé and Hartmann, 1997; Von Salzen et al., 2005; Boutle et al., 2011). In the absence of shallow convection, moisture levels in the free troposphere would be disconnected from that in the boundary layer (Neggers et al., 2007). The moisture that shallow convection transports is responsible for fuelling deeper convection, and thus driving larger scale circulations. The study by Holloway and Neelin (2009) focused on water vapour in atmospheric columns, and its relation to tropical deep convection. It was concluded from this study that shallow convection controls the moisture above the boundary layer which is crucial for deep convection and precipitation processes.

Further studies show that deep convection depends on humidity levels in the lower troposphere, and that shallow convection controls this moisture (Esbensen, 1978; Wu et al., 2009; Zhang and Klein, 2010; Cai et al., 2013). There are numerous studies that delve into the processes by which shallow convection preconditions the atmosphere for deeper convection. Wu

et al. (2009) discusses how shallow convection preconditions the atmosphere through evaporative cooling. The evaporation of cloud droplets in boundary layer cloud into the surrounding air cools and moistens the atmosphere locally. This has two effects – firstly, the moistening of the environment and a reduction of its stability, and secondly, the lessening of cloud dilution from the environment. As a result, the buoyancy of the environment decreases. When the cloud becomes positively buoyant with respect to the environment, a transition from shallow into deep convection occurs (Wu et al., 2009). Another factor that triggers the transition from shallow to deep convection are heterogeneities in the boundary layer (Zhang and Klein, 2010). The buoyancy of an air parcel increases with increased variance in temperature and humidity. In summary, boundary layer inhomogeneity, tropospheric lapse rate, and humidity are all factors which control the transition from shallow to deep convection.

The control that shallow convection has on tropospheric humidity levels and the associated transport of moisture is a crucial component of climate dynamics. Subtropical shallow convection interacts strongly with large scale tropical circulations and in particular there is a connection between shallow convection and the inter-tropical convergence zones (ITCZs) (Siebesma, 1998; Frierson, 2007). Through horizontal advection, shallow convection transports moisture from subtropics into the tropics. Tropical climate modelling shows that a reduction of shallow convection leads to a drying in the free troposphere, and an overly moist boundary layer (Neggers et al., 2007). Reduction of shallow convection weakens deep convection and precipitation on the edges of ITCZs. Shallow convection therefore affects the width and intensity of the ITCZ through moisture transport from the boundary layer to the free troposphere, and increased surface evaporation.

In addition to climate dynamics, the contribution of shallow convection within weather forecasting is significant. Early work shows that Numerical Weather Prediction (NWP) model skill increases greatly with the inclusion of shallow convection (Tiedtke et al., 1988). The study by Tiedtke et al. (1988) portrayed how the addition of physics to represent non-precipitating shallow cumulus to the European Centre for Medium-Range Weather Forecast's (ECMWF) forecast model improved the forecast by increasing the moisture transport from subtropics into convergence zones. This introduction of shallow convection to the forecast resulted in a deepened moist layer with shallow cumuli at the top of the boundary layer. It was also discovered that in comparison to the other model modifications made at this time, it was the addition of the shallow convection parameterisation that produced precipitation results closest to that of the climatology, particularly at the ITCZs. A more recent study by Bechtold et al. (2014) explored the role shallow convection plays in the ECMWF Integrated Forecasting System (IFS). IFS integrations were run by altering or swapping out the shallow convection scheme. The integrations outputted the global cloud distribution, with shallow convective clouds accounting for up to 90% of the cloud type in the subtropical anticyclonic regions. The study concluded that an omission of shallow convection results in an overestimation of boundary layer moisture content and boundary layer cloud levels. It is clear that shallow convection has implications

for both short-term NWP and long-term climate dynamics.

With regards to future outlook, work has been done to determine the role shallow convection will play within a warmer, more humid climate. A global weakening of the large scale atmospheric circulations, the Hadley Cell and particularly the Walker Cell, is indicated by climate models (Vecchi and Soden, 2007; Su et al., 2014). However this may not be the case regionally. Simulations from tropical climate models show that in a warmer climate, shallow convection increased the vertical velocity at 500hpa (Chou and Chen, 2010). Research shows that regions where the troposphere on average has a "bottom heavy" vertical structure (the majority of vertical motion occurs in lower troposphere, i.e. shallow convection) are to favour deep convection in warmer climate (Chen et al., 2016). These regions are projected to experience a strengthening in vertical ascent, and therefore circulation. In other words, shallow convection will be associated with increased tropical convection in a warmer climate. Therefore, when projecting regional precipitation changes in the tropics, regions where shallow convection is prevalent should be taken into consideration.

1.1.2 Modelling Shallow Convection

As outlined in the previous section, it is clear that shallow convection plays a role in numerous aspects of the climate system. Good representation of shallow convection in models is necessary for the production of realistic forecasts and future climate projections. It is crucial that General Circulation Models (GCMs) and NWP models account for shallow convection and represent it successfully in our present-day climate, before an accurate simulation can be made of our potential future climate. Shallow convection occurs on a scale too small to be explicitly resolved by GCMs, thus parameterisation schemes are used to represent it instead. Unfortunately, parameterising shallow convection is not straight forward, as it encompasses many different processes that interact with each other simultaneously, including turbulent mixing, radiation processes and cloud condensation processes. Further complexity arises due the difference in the behaviour of certain processes (e.g. turbulence) within the subcloud layer to that within the cloud layer.

Decades of work have gone into the development of shallow convection schemes that are used today in operational NWP models and in climate models. The inclusion of shallow convection parameterisation is necessary to represent the transport of heat and moisture which drive large scale circulations. Schemes that describe shallow convection are distinct from those for deep convection, with processes such as turbulent mixing and surface evaporation being more prominent in the dynamics of shallow convection. In the past, some models neglected to incorporate any shallow convection amongst their schemes. One of the first approaches in accounting for shallow convection within large scale atmospheric models was a mass-flux technique. Early development of shallow cumulus convection schemes discovered that the vertical mass-flux of cloud determined the thermodynamic evolution of the environment (Arakawa

and Schubert, 1974). Arakawa and Schubert (1974) developed a parameterisation closure to be used in models that used budget equations for water, mass and moist static energy to describe how cumulus modified the large scale environment. Parameterisation schemes using a mass-flux approach were furthered developed and verified through field experiments (Tiedtke, 1989). This mass-flux scheme described by Tiedtke (1989) has since been used widely and adapted to operational NWP models, such as at the ECMWF forecast model.

Aside from mass-flux techniques, other approaches for the parameterisation of shallow convection include a combined eddy-diffusivity and mass-flux (EDMF) closure (Siebesma et al., 2007). The EDMF approach developed by Siebesma et al. (2007) uses a mass-flux closure to describe organised updrafts driven by thermal forcings within a dry boundary layer. Corresponding subsidence was treated as turbulent motions using an eddy-diffusivity closure. This EDMF technique was adapted by the ECMWF model to describe dry convective boundary layers. Other convection parameterisation schemes include plume models, which represent the entrainment and detrainment associated with convective plumes to determine realistic moisture and mass-flux profiles (Kain and Fritsch, 1990). Statistical techniques are utilised in some stochastic parameterization schemes for convection in which probability density functions are used to determine the probability of a convective plume occurring in a grid box (Plant and Craig, 2008). This stochastic scheme described by Plant and Craig (2008) also incorporates a plume model to represent the plumes.

All of the various types of convective parameterisation schemes use closures to approximate subgrid dynamics given a set of assumptions. Evaluations are required for the verification of schemes and to test whether these assumptions are suitable. However, early evaluations of shallow convection schemes showed that the assumptions were not precise. As a result, the parameterisation schemes are not performing well and GCMs are struggling to capture shallow convection perfectly. Comparisons of model outputs with observations highlight the deficiencies of the parameterisation schemes. In particular, two shortcomings of GCMs today are under representation of shallow cloud cover and the early onset of precipitation.

A project comparing cloud variation as modelled by 10 different GCMs to satellite observations found that low lying cloud is under represented (Zhang et al., 2005). Results from this comparison showed that 5 out of the 10 models under-estimated the amount of low cloud. On average, the models were found to have 70%-80% of the amount of cloud that was observed by satellite. Another GCM intercomparison study of global cloud regimes by Williams and Tselioudis (2007) found that all the models poorly simulated shallow cloud, notably trade wind cumuli in the tropics. In comparison to observations, the presence of shallow cumulus in some models was too low, and satellite uncertainty could not account for the inconsistency. This underestimation of boundary layer clouds by GCMs poses an issue due to the radiative contribution of boundary layer cloud and cloud feedbacks.

Another study comparing model simulations to a 30 year set of observations revealed the failure of shallow convection schemes in representing precipitation cycles (Dai et al., 1999). The

study modelled diurnal cycles of precipitation during Summer in the US with three different shallow convection parameterisations. None of the schemes were successful in capturing the observed diurnal cycles. The model produced rainfall too early in the day, too often and at a lower intensity than that observed. The early onset of rainfall was an error that arose in all three schemes. It was suggested from this study that the criteria for moist convection was too weak, resulting in an overestimation of cloud cover which reduces surface heat flux and therefore weakening the diurnal cycle. It was concluded that further work was required to improve moist shallow convection schemes and cloud schemes, with regards diurnal cycles. The early onset of rainfall is not unique to this study, and seems to be a common failure of shallow convection schemes within global models. This early onset of rainfall was further explored by Bechtold et al. (2004), in which Cloud Resolving Model (CRM) simulations of diurnal convective precipitation are compared to various ECMWF convection schemes in Single Column Models (SCMs). The early onset was suggested to be a failure of the schemes to account for the growth period from shallow to deeper convection. Since this study, more modern mass-flux closures have been developed (Plant and Yano, 2016). Running the ECMWF forecast model with the most modern mass-flux schemes has shown to reduce this early onset of rainfall in these diurnal cycles, although in some regions there remains a lag of 2 hours between peak simulated rainfall, and that observed.

It is important to be able to predict the diurnal cycle of shallow convection and therefore rainfall, as it is a major mode of precipitation variability for many regions across the world. It is clear that further development of parameterisation schemes is required. To create accurate schemes, the assumptions and approximations incorporated within the schemes need to be realistic. Determining realistic assumptions and closures requires a thorough understanding of the physics involved in shallow convection, at all stages of its life cycle. Approximations that hold for the early-stage of cloud development, may not be suitable during the mature stage of development or when the clouds are in their decay stage. The following section will focus on the studies which have sought to gain a deeper understanding of the life cycle of shallow convection.

1.2 Diurnal Cycle of Shallow Convection

In this section, key pieces of work on the diurnal cycle of shallow convection that have led to the development and improvement of parameterisation schemes are reviewed. Previous studies have shown how Large Eddy Simulations (LES) are valuable tools for researching the dynamics associated with boundary layer convection. LES models do not require a parameterise for convection, as the resolution is high enough for convection to be explicitly resolved. For this reason LES enables the atmosphere to be represented in a way that is reflective of observations and reality, but also can be used as a dynamic model to simulate physical processes

on a consistent three dimensional grid (Gustafson et al., 2017). LES models incorporate parameterisation schemes for subgrid dynamics and microphysics, and therefore can be sensitive to these schemes. Here, focus is given to studies of the diurnal cycle of oceanic shallow cumuli in trade wind areas (Siebesma and Cuijpers, 1995; Stevens et al., 2001), and studies of shallow convection over land (Brown et al., 2002; Lenderink et al., 2004; Chlond et al., 2014; Fast et al., 2019).

1.2.1 Shallow Convection Over Seas

The early studies on shallow convection were devoted to understanding the behaviour of the shallow cumuli found in trade wind regions. The study by Siebesma and Cuijpers (1995) was the first concrete analysis which dissected the processes involved with oceanic shallow convection. Shallow non-precipitating cumuli which were observed as part of the Barbados Oceanographic and Meteorological Experiment (BOMEX) were simulated. The goal of this work was to investigate whether the assumptions used in parameterisation schemes for trade shallow cumuli were realistic. An LES model was used to simulate a reconstruction of the diurnal cycle of summertime convective cumulus as observed during a period within BOMEX. The results from the simulations were scrutinised and the characteristics of the convection were broken down. In particular, focus was given to the fluxes associated with convection, including potential temperature, buoyancy, moisture, and vertical velocity fluxes. The detail obtained from the shallow convective dynamics was used to critique the parametric assumptions operating in models at the time. The aims were to evaluate a scheme used to represent turbulence, and to verify the rates used for entrainment and detrainment. The turbulence scheme under scrutiny was one that approximated all turbulence associated with convection as an updraft and corresponding subsidence. The fluxes simulated by the LES model were higher than that estimated by the scheme, notably potential temperature fluxes were greatly underestimated by the turbulence scheme. It was thought that this discrepancy was due to failure of the scheme to account for unorganised turbulence found in-cloud or in the environment. Furthermore, the results showed that a scheme that included the specification of "core" points in addition to cloudy and environmental points produced the best results, although magnitudes for the fluxes were still too low. Core points refer to cloudy points that have positive vertical velocity and are positively buoyant with respect to the environment. The categorisation of core points within the diagnostics is an approach that has been adopted and used in studies. The LES results were important as they recreated the interaction between clouds and the environment. The exchange of mass of clouds with the surrounding air through entrainment and detrainment impacts cloud development, and can result in the growth or suppression of clouds. In parameterisation schemes the accuracy of the representation of clouds within models depends on the precision of prescribed entrainment and detrainment rates. The work by Siebesma and Cuijpers (1995) found that the rates prescribed within models at the time were a magnitude lower than that simulated

by the LES. Models therefore produced clouds at unrealistically high levels. The simulated detrainment rates were lower than entrainment rates, meaning that the clouds lose mass from cloud-base to top. This result contrasted with the assumption used at the time that entrainment occurred only at cloud-base, and detrainment at cloud-top. This study allowed for the refinement of the parameterisation closures being tested.

Following on from this work was another study on shallow trade cumuli that sought to understand the dynamics of such convection under a strong inversion. The study by Stevens et al. (2001) was an intercomparison study of LES simulations using observations from the North Atlantic as part of the Atlantic Trade Wind Experiment (ATEX). This observational region is further downstream than that of BOMEX, where the shallow convection formed a layer of stratocumulus under a strong temperature inversion. The initial conditions for this case was similar to that from BOMEX, although in the mixed layer, humidity decreased from $17 \mathrm{gkg}^{-1}$ as was in BOMEX, to $12 \mathrm{gkg}^{-1}$. The potential temperature in the mixed layer was also about 3K lower than that in the BOMEX case, with a much sharper capping inversion at approximately 1500m. Generally, the intercomparison found good agreement between the simulated profiles of mass-fluxes, the evolution of thermodynamic properties and cloud fraction. The analysis of convective processes below the stratiform layer was consistent with that determined by Siebesma and Cuijpers (1995) in the BOMEX case. However, it was found that the presence of the stratiform layer produced a radiative feedback which drove small-scale circulations in the free troposphere above the cloud top. These circulations increased the heat and moisture transport from the cloud layer into the free troposphere. The mass-flux schemes used struggled to capture this cloud-radiation interaction. It was concluded that the subcloud layer was well represented by the mass-flux scheme, however due to the dynamics of the stratiform layer, the parameterisation schemes failed to portray certain fluxes in the upper cloud layer. This paper deduced that more work was required with regard to mass-flux schemes. In particular, it was suggested that a scheme which allowed for a coupling of the subcloud layer, cloud layer, and the free troposphere would be necessary to get the most realistic representation. The data sets from both of these studies have proved to be very useful in gathering a more complete picture of shallow convection in a trade wind regime. However, even under modern modifications to parameterisations in recent years, trade wind stratocumuli are still found to be too reflective in the ECMWF forecast model due to an overestimation of liquid water content (Plant and Yano, 2016). This implies that future work is still required to represent these processes fully.

1.2.2 Shallow Convection Over Land

Convection over land differs from that over sea, namely as the diurnal cycle of temperature and heat flux is much stronger. This was the motivation for the study made by Brown et al. (2002), who explored the dynamics within a diurnal cycle of shallow convection over land. The investigation was an intercomparison of eight different LES models, which simulated a single

diurnal cycle of shallow convection. The models were based on idealised observations from the Atmospheric Radiation Measurement (ARM) facility in the Southern Great Plains (SGP) in the USA. Over land, surface forcings for sensible and latent heat fluxes are stronger both in terms of magnitude and their diurnal cycle, than that over seas. The Bowen ratio specifies the relative strength of sensible to latent forcing, as it is the ratio of sensible heat flux to latent heat flux. Over land case, the Bowen ratio is approximately 0.3, while the BOMEX and ATEX cases described in Section 1.2.1 had a Bowen ratio of approximately 0.06. Aside from stronger surface forcings, the ARM case has an initially more stably stratified atmosphere. Unlike the BOMEX and ATEX cases, a clear conditionally unstable layer above the boundary layer cannot be seen in the initial potential temperature profile. Brown et al. (2002) compared the evolution of clouds to that in the BOMEX case. In general, the main differences were higher cloud-base and cloud-tops, higher core fraction and increased mass-flux. Unlike the BOMEX and ATEX cases which had a relatively constant cloud fraction, over land clouds rapidly develop and reach their peak in cloud fraction soon after appearing, before a gradual decay as they dissipate. Peak cloud fraction was approximately 0.3, compared to just 0.15 in the BOMEX simulations. Peak mass-flux was found to be almost 3 times that in the BOMEX case. These differences are explained by the difference in the strength of forcing. The structure of turbulence in the dry convective layer and subcloud layer was similar to that described in the BOMEX case. Numerical sensitivity tests did not affect the overall results and there is a robust agreement between all the LES models, as they showed little spread in their results.

The data from this case study have been used in many later papers as a benchmark for the assessment of parameterisation schemes. In particular, these LES results were used to evaluate parameterisation schemes that were tested on seven different SCMs (Lenderink et al., 2004). SCMs are beneficial for trialing parameterisation schemes as a single column allows the separation of physics scheme error from GCM uncertainty. In contrast to the agreement between the LES results in the work of Brown et al. (2002), the outputs from the seven SCMs were highly dissimilar. There was a large spread in results, with main differences occurring in the values of cloud cover, cloud liquid water, thermodynamic profiles, as well as a presence of numerical noise. The SCMs varied from one another in terms of the closure schemes used within the parameterisations. The convection scheme, cloud scheme and turbulence scheme were found to be responsible for the spread of results. Cloud cover was overproduced too early during the simulation, and clouds did not dissolve at the end of the day, in contrast to the LES simulations. The SCMs overestimated liquid water path, with an output 2 to 5 times higher than that from the LES results. The SCMs could not agree on the evolution of potential temperature profiles. Unrealistic wind velocities were also produced. These issues and behaviours were narrowed down and categorised as a result of either too strong turbulent activity or too strong mass-flux activity. These schemes were modified, and simulations re-run with the updated schemes. The results were improved, with a reduction in cloud cover and more realistic thermodynamic and

mass mixing ratio profiles were outputted. This study is just one example of how LES simulations can provide many detailed diagnostics which would be difficult or impossible to obtain directly from observations. Thus, data from LES simulations can be used as a benchmark for the evaluation of parameterisation schemes.

More recent research studies using LES simulations based on ARM observational campaigns explore factors that impact the development of clouds, both meteorological and non meteorological. The study by Stirling and Petch (2004) investigated the impact convectively generated temperature and humidity variability has on the diurnal cycle over land. They concluded that horizontal temperature and moisture heterogeneities generated by deep convective events from a prior diurnal cycle had an impact on subsequent convection. In particular, they found that convective activity simulated by LES models was advanced by 1 to 3 hours with the inclusion of this spatial variability, and rainfall increased by up to 70%. It was also discovered that initial moisture variability has more of an impact on the convection than variability in temperature. In addition, boundary layer variability influences the deepening of convection more than variability in the free troposphere. It was thought that fluctuations in humidity and temperature in the boundary layer act to overcome the convective inhibition to allow for the release of convective available potential energy and thus deepening of convection. CRMs forced with observations of diurnal cycle of shallow convection ideally should be initiated with any observed variability. An intercomparison of CRMs simulating observed summertime convection at the ARM site found that many models were delayed in their production of rainfall (Xu et al., 2002). It is possible that the inclusion of initial spatial variability may improve this delayed onset of precipitation in CRMs.

Meteorological factors such as initial humidity and atmospheric stability are therefore known to have an influence on cloud depth, and cloud fraction. However non-meteorological variables including surface inhomogeneities, soil moisture content and aerosols as well as numerical factors also have significant effect on the development of the boundary layer and/or cloud development. Activities such as agriculture and other forms of land use have an impact on temperature and air circulation, which in turn influence shallow convection (Fast et al., 2019). Boundary layer development has a dependence on soil moisture content which also interacts with initial humidity and atmospheric stability to influence the development of shallow convection (Chlond et al., 2014). The diurnal cycle of shallow convection as simulated by CRMs is further dependent on the numerical set up of model. Horizontal resolution must be high enough such that gridspacing is no greater than one quarter than that of the depth of the subcloud layer (Petch et al., 2002). The paper by Petch et al. (2002) concluded that insufficient horizontal resolution impedes the transport of heat and moisture from the boundary layer into the free troposphere, and results in the delay of convection in CRMs. Therefore, adequate resolution is necessary for LES models to correctly represent the diurnal cycle of shallow convection. In addition, it is clear that the inclusion of initial atmospheric variability more advanced parameterisation schemes that represent subgrid land variability will improve the representation

of shallow convection within models.

These pieces of literature have provided essential information for the direct improvement of parameterisation schemes. Further refinement within schemes is still required. Although the work by Chlond et al. (2014) did look at sensitivities to initial conditions, this was done in conjunction with modifying surface soil moisture and did not discuss the evolution of shallow cloud as purely a function of initial atmospheric conditions. This leads to the question of how does a change in initial environment, namely initial humidity and atmospheric stability, impact the development of shallow cumulus. The study by Stirling and Petch (2004) determined the influence of variability generated by deep convection on the diurnal cycle of shallow convection. It is not known if variability generated from a previous cycle of shallow convection influences the subsequent development of convection in the same manner. These questions motivate the goals of this dissertation, which are stated in the following section.

1.3 Project Goals

Understanding shallow convection and its life cycle is of great benefit for both daily forecasting and for long-term future climate projections. Although many advancements have been made over recent decades, comparison of GCM output with observations suggests that improvements are still required with regard to parameterisation schemes. An LES study is a good approach for gaining a deeper understanding of precise atmospheric dynamics, which is required for development of model closures. There are many in-depth analyses with regards shallow convection in oceanic trade wind regions, however understanding shallow convection over land is less explored. This motivates this dissertation, as the overall goal is to understand the diurnal life cycle of shallow convection over land. The new Met Office NERC Cloud model (MONC) is a CRM and has never been used to simulate the diurnal cycle of shallow convection. The first aim of this dissertation is to evaluate MONC's simulations against observations and against other LES simulations of the diurnal cycle of shallow convection. To approach this, the model will simulate a single diurnal cycle of shallow convection with the same initial conditions and parameters as used in the previous literature for the ARM case. This control simulation will be used as a comparison against simulations described by Brown et al. (2002). Following this, this dissertation will explore the model sensitivities to initial conditions. In particular, what impact the initial humidity has on the evolution of clouds during the life cycle of shallow convection. Similarly, what impact the initial atmospheric stability (i.e. initial potential temperature profile) has on the formation of clouds. By answering these questions, one can discover which (if any) of these initial conditions is most dominant in controlling the evolution of shallow convection. The final aim is to determine how the diurnal cycle of shallow convection behaves on a second consecutive day. In other words, how will the model respond to increased thermodynamic variability within the domain, and what impact will this have on the cloud development and properties. To answer these questions, a series of simulations will

be run using the new Met Office NERC Cloud model and an analysis of the diagnostics will be given.

Details about the Met Office NERC Cloud model are given in Section 2, the description of the control simulation is given in Section 3, the results from varying the initial domain-mean humidity conditions are given in Section 4, the results from varying the initial domain-mean potential temperature conditions are given in Section 5, the results from investigating the initial horizontal thermodynamic variability are given in Section 6, and a summary of the main conclusions and possible extensions of this work are given in Section 7.

2 New Met Office NERC Cloud Model

This section will provide some background on the new Met Office NERC cloud model. An overview of the model's governing equations and subgrid parameterisation schemes is described.

2.1 Model Background

The new Met Office NERC Cloud model (MONC) is a high resolution cloud resolving numerical model (Brown et al., 2015). This model has an expansive range of scientific uses including the simulation of dry and moist convection and related processes under a variety of scales. The model is sophisticated through its coupling of cloud microphysics and radiative schemes. Prior to this project, it has not been used for simulating the diurnal cycle of shallow convection.

MONC is a rewrite and modernisation of the Met Office Large Eddy Model (LEM) (Gray et al., 2001). As an improved version of the LEM, its rewrite included improvements of the software, scalability and code parallelisation (Brown et al., 2015). MONC simulates atmospheric and fluid dynamics through the solution of a governing set of equations. It explicitly resolves large turbulent eddies and resolves the associated mass and energy transport. Subgrid turbulence such as smaller dissipative eddies can be represented in the model through turbulence parameterisation schemes. Other schemes included in the model are a cloud microphysics scheme, and a radiation scheme.

2.2 Governing Equations

The prognostic variables which are resolved in the model include the three dimensional velocity vector ($\mathbf{u}$), potential temperature (θ) and scalars (q_n) which include the mixing ratios for water species. The model determines these prognostics by solving differential equations, known as the Boussinesq set of equations. Under the Boussinesq approximation, potential temperature, pressure (p) and density (ρ) fields are linearised as perturbations acting on a reference state. The model acts to solve these perturbations, given a specified reference potential temperature state. The model can be configured to run under the Boussinesq approximation, in which

the reference state is constant, or under the anelastic approximation, in which the reference state is a function of height solely.

The set of governing Boussinesq equations includes the Navier-Stokes equation (Equation 2.1), the continuity equation (Equation 2.2), a thermodynamic equation (Equation 2.3) and a prognostic equation for the n^{th} scalar (Equation 2.4). Tensor notation is as standard.

$$\frac{Du_i}{Dt} = -\frac{\partial}{\partial x_i}\left(\frac{p'}{\rho_s}\right) + \delta_{i3}B' + \frac{1}{\rho_s}\frac{\partial \tau_{ij}}{\partial x_j} - 2\epsilon_{ijk}\Omega_j u_k \tag{2.1}$$

$$\frac{\partial}{\partial x_i}(\rho_s u_i) = 0 \tag{2.2}$$

$$\frac{D\theta'}{Dt} + w\frac{d\theta_s}{dz} = \frac{1}{\rho_s}\frac{\partial h_i^{\theta'}}{\partial x_i} + \frac{1}{\rho_s}\frac{\partial h_3^{\theta_s}}{\partial z} + \left(\frac{\partial \theta'}{\partial t}\right)_{mp} + \left(\frac{\partial \theta'}{\partial t}\right)_{rad} \tag{2.3}$$

$$\frac{Dq_n}{Dt} = \frac{1}{\rho_s}\frac{\partial h_i^{q_n}}{\partial x_i} - \left(\frac{\partial q_n}{\partial t}\right)_{mp} \tag{2.4}$$

The temperature perturbation is denoted by θ' and the mean reference states of potential temperature, density and pressure are denoted as θ_s, ρ_s and p_s respectively. Subscripts "mp" and "rad" denote microphysics and radiation source terms respectively. The variable h^X is the subgrid flux of the variable X. Buoyancy is denoted by B', and is defined as follows.

$$B' = g\frac{\theta'_v}{\theta_s} \tag{2.5}$$

θ'_v is the perturbation of virtual potential temperature. The model calculates θ'_v using Equation 2.6. The number "c_n" is a coefficient which is a measure of the influence of q_n on the density of an air parcel.

$$\theta'_v = \theta + \theta_s c_{n,i} q_{n,i} \tag{2.6}$$

The mean reference states of density and pressure are determined by applying hydrostatic balance (Equation 2.7) and the ideal gas law (Equation 2.8).

$$\frac{dp_s}{dz} = -g\rho_s \tag{2.7}$$

$$p_s = \rho_s R\theta_s \left(\frac{p_s}{p_0}\right)^{\frac{R}{C_p}} \tag{2.8}$$

The constants R and c_p are the universal gas constant and specific heat capacity of air at constant pressure, respectively. A reference value for pressure which is specified by the user is denoted by p_0. The reference states of p_s and ρ_s can be determined from Equations 2.7 & 2.8

given one set of boundary conditions, chosen as the value of pressure at the surface. The model therefore solves the prognostic variables of the three-dimensional velocity vector, the potential temperature perturbation and the scalar fields of water species by performing forward-in-time integrations over this equation set.

2.3 Model Configuration

The model can be configured to run in two dimensions or as a three-dimensional model. Horizontal grid spacing is constant, however vertical grid spacing can be adjusted to have varying resolution. The model uses periodic boundary conditions in the horizontal. In the vertical, the top and bottom surfaces act as rigid lids, across which no transport is resolved. The top rigid lid may produce gravity waves as a result of reflection at the boundary. To prevent this, the model can be set to include damping at upper vertical levels. With damping enabled, prognostics are relaxed to their mean values above a prescribed height.

Surface forcings on the lower lid can be prescribed, to represent surface fluxes or surface stresses. Surface conditions can be set via a prescribed flux, or by fixing temperature and/or humidity at the surface. A sea surface can also be established by fixing surface humidity to be at saturation. The surface conditions can be chosen to vary in time. The model also includes two different large scale forcings schemes, which can be enabled to advect model prognostics. Prescribed large scale tendencies can also be configured for simulations. Other model parameters include subgrid schemes to represent unresolved eddies. Diffusivity and viscosity processes can be enabled. In addition, a backscatter scheme to improve the representation of turbulence can be switched on or off.

The model also includes a radiation scheme which represents interactive radiation processes such as absorption, reflection and scattering (Edwards and Slingo, 1996). Optical processes and scattering specific to hydrometeor species is also described by this scheme, and a parameter exists that controls whether the radiation scheme can interact with hydrometeor species. Radiation frequency, solar constant and angle of solar radiation can be controlled, in addition to the selection of long-wave or short-wave radiation. The radiation scheme can be switched on or off, and prescribed radiation forcing can also be set.

2.4 CASIM

If the model is chosen to simulate moist processes, a cloud microphysics scheme is used to compute and represent moist particle interactions and physics. The microphysic scheme used by MONC is the newly developed Cloud Aerosol Interactions Microphysics Model (CASIM) (Brown et al., 2017). CASIM is user-configurable and the representation of various hydrometeor species can be selected, including rain, snow, ice, liquid cloud water and graupel. CASIM is a bulk scheme meaning that water species particles are described in terms of diameter, shape,

slope and distribution. It is a three-moment scheme, in which the particle slope is fixed, and diameter, distribution and shape are defined within the scheme. Moist processes can be extremely complex to represent as they include phase changes, particle collisions and coalescence, nucleation and aggregation and autoconversions of the hydrometeors. CASIM therefore undergoes computationally intensive calculations to describe these various interactions. CASIM has an advantage over similar microphysics models due to its handling of aerosols.

The enabling of the aforementioned schemes and adjustment of the model parameters are defined within a configuration file that is read into the model. The model set up is specified in this file including the definition of the domain size, length of run, and whether the simulations are moist or dry. The initial conditions of reference potential temperature, surface pressure, reference pressure, Coriolis force and initial profiles of temperature and humidity conditions are also prescribed in this file. The model outputs diagnostics at a designated frequency. Conditionally sampled diagnostics can be outputted which meet a prescribed condition, such as gridpoints which are buoyant or have cloud. The description of the model configuration and set up used for the purpose of this dissertation is given in the following section.

3 Control Simulation

The following section describes the results from modelling a single diurnal cycle of shallow convection over land. The simulation is initialised with conditions and parameters consistent with that done by Brown et al. (2002). The model output is analysed focusing on cloud development and the evolution of atmospheric conditions. A comparison of results is made to that found by Brown et al. (2002) to evaluate the performance of MONC and determine whether MONC can suitably model shallow convection. This simulation is referred to as the control simulation.

3.1 Model Set Up

The model is set up to reconstruct the formation of summertime shallow convection on a clear boundary layer, as observed at the ARM central facility, in Oklahoma USA. The settings and parameters are chosen to be identical to that in the simulations run by Brown et al. (2002). The model is selected to operate in a three-dimensional (3D) configuration, under the anelastic approximation. The domain size is set as 64 x 64 gridpoints in the horizontal, and 110 levels in the vertical. Resolution is chosen to be 100m in the horizontal, and 44m in the vertical, forming a 3D domain of 6400 x 6400 x 4400 m^3. The model run time is set at 64800s, such that simulations are run for an 18hour period, from 1130UTC to 0530UTC (local time of 6.30am to 12.30am).

The initial profiles of humidity and potential temperature for the control simulation are prescribed, using idealised observations recorded at the ARM facility on the 21 June 1997. The initial profiles are shown in Figure 3.1a. Initially, the mean surface potential temperature is 299.5K, and there is a small surface inversion. From 700m up to the capping inversion at 2.5km, there is a lapse rate of 5.72Kkm^{-1}. The initial mean total mass mixing ratio at the surface is 15.53gkg^{-1}. This decreases with height gradually, up until 1300m. Thereafter, the mass mixing ratio sharply decreases to 3gkg^{-1} at 2500m, and remains constant with height. The values used for the initial thermodynamic profiles are listed in the Appendix A.1. A more detailed description of the selection of these initial conditions can be found in Brown et al. (2002). Reference pressure is

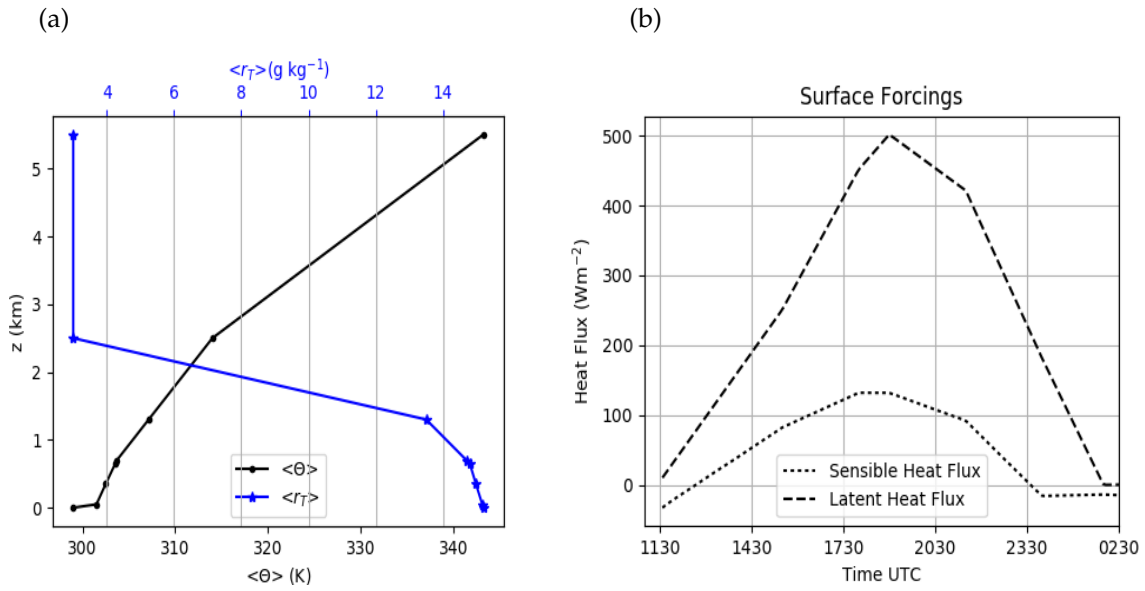

Figure 3.1: (a) Initial humidity and potential temperature profiles used for the control simulation, from Brown et al. (2002). (b) Time series of the imposed surface forcings of sensible and latent heat fluxes, peaking between 1800UTC to 1900UTC (1.00pm and 2.00pm local time).

defined as 100000Pa and surface pressure is specified as 97000Pa. Reference potential temperature is set as 299K. The Coriolis force is set to 8.5x10^{-5}s^{-1}, and geostrophic wind is set as (u, v) = (10ms^{-1}, 0) and remained constant throughout the simulation.

Surface boundary conditions are prescribed to be time-varying fluxes that are horizontally homogeneous. The model is forced by prescribed surface heating and moistening through sensible and latent heat fluxes which vary during the day as shown in Figure 3.1b. Peak values are reached at 1830UTC (afternoon local time), representing maximum solar heating. After 2300UTC (6.00pm local time), the sensible heat forcing becomes negative, representing nightfall. The model's large scale advection schemes, backscatter scheme and the radiation code are disabled. Large scale advective forcings and radiative tendencies are instead prescribed. These forcings act to balance the surface forcings. They include advective tendency of mean potential temperature (A_θ), radiative tendency of mean potential temperature (R_θ), which are applied to the θ equation, and advective tendency of mean mass mixing ratio (A_{r_T}) which is applied to the r_T equation. These tendencies are applied below 1km. Above 1km, the magnitude of these tendencies is reduced linearly from the value at 1km, to a magnitude of zero at 2km. No forcing is applied above 2km. The profiles of these tendencies at different times can be found in the Appendix A.1. CASIM is configured to represent the hydrometeor species of rain, liquid cloud and water vapour.

Diagnostics are outputted at 5 minute intervals. The following are the definitions of the conditional sample diagnostics used for the simulations. Cloudy points are defined by gridpoints with specific humidity of liquid cloud q_l > 1x10^{-5} kgkg^{-1} or ice q_i > 1x10^{-5} kgkg^{-1}.

Buoyant points are defined by gridpoints which have a positive virtual temperature perturbation with respect to the layer mean ($\theta_v' > 0$). Updrafts are defined by gridpoints with a positive vertical velocity ($w > 0$). This simulation with this model set up will be referred to as the control simulation, and results are analysed below.

3.2 Evolution of Mean Potential Temperature and Mixing Ratio

The vertical profiles of the horizontal mean potential temperature ($<\theta>$) and horizontal mean total mass mixing ratio ($< r_T >$) are first examined. These describe how the domain-mean temperature and moisture content of the atmosphere evolves throughout the day. The variable r_T is the sum of the mixing ratio of liquid water and the mixing ratio of water vapour. Profiles are shown at three-hourly intervals throughout the simulation, in Figure 3.2. This is compared to the results obtained from the ensemble of CRMs as studied by Brown et al. (2002) shown in Figure 3.3.

The top panel of Figure 3.2 shows the domain-mean potential temperature. The boundary layer is identified by the depth of atmosphere from the surface where $<\theta>$ is almost constant with height. The boundary layer depth grows steadily as the day goes on, reaching a depth of almost 1km by 1730UTC. It grows as the surface flux increases throughout the day, inducing mixing within the lowest layer of the atmosphere. From 1730UTC to 2030UTC, shallow convective activity causes a decrease in the potential temperature of up to 1K in the free troposphere between 1.5km and 2.5km. By the end of the next three-hourly period at 2330UTC, the mean potential temperature in this depth has further reduced by 1K. This reduction in free tropospheric lapse rate shows that the free troposphere is becoming more unstable. This layer of reduced stability is capped with an inversion at 2.5km. The evolution of the $< \theta >$ is in agreement with that given by Brown et al. (2002), as seen in Figure 3.3.

Similarly, the evolution of $<r_T>$ throughout the simulation period corresponds well with that found by Brown et al. (2002). The mass mixing ratio in the boundary layer experiences a sharp increase of 2gkg^{-1} near the surface after the first three hours by 1430UTC. Moisture content of the boundary layer continues to build up, consistent with the increasing surface latent heat flux. Humidity in the free troposphere above the boundary layer can be seen to develop from 2030UTC onwards. There is an increase of up to 3.5gkg^{-1} by 2330UTC and at this time the moisture content in the boundary layer has decreased slightly. This evolution is evidence of the shallow convection transporting moisture from the boundary layer, into the free troposphere, and eventually drying the boundary layer.

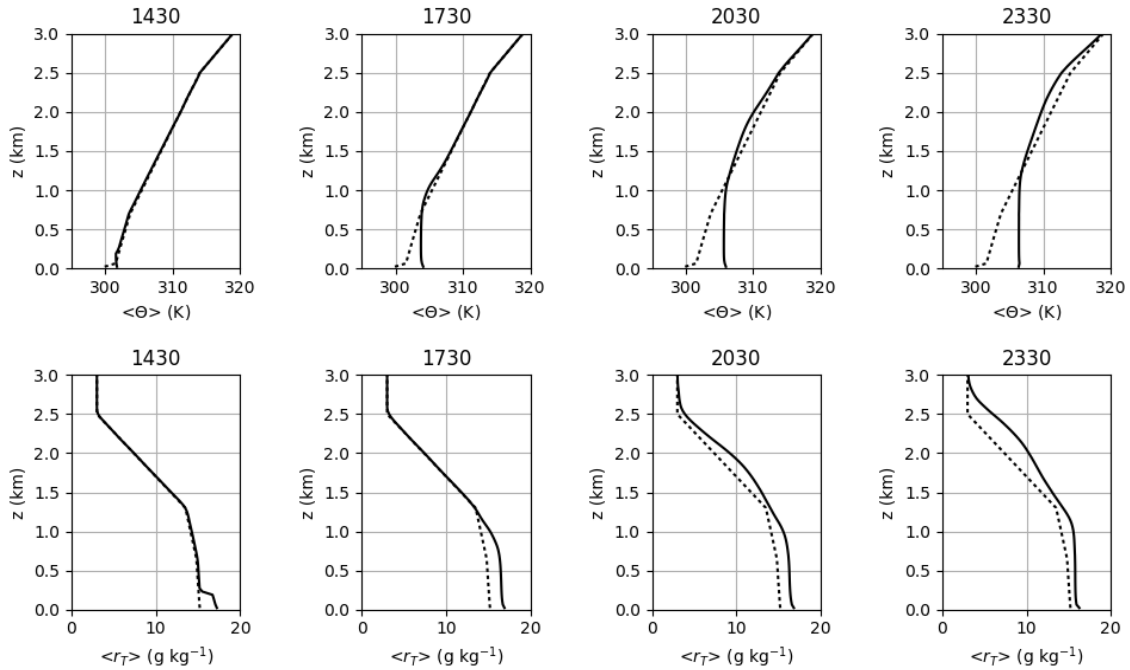

Figure 3.2: Domain-mean potential temperature $<\theta>$ and mass mixing ratio $<r_T>$ profiles at four different times during the control simulation. Dashed line represents the initial profile used during the simulation.

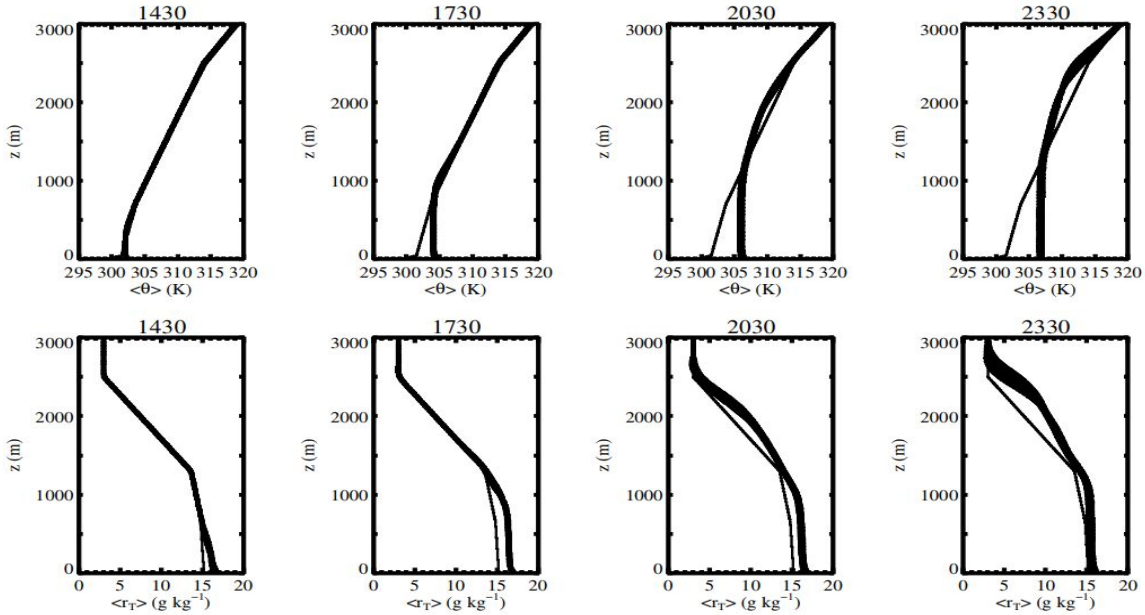

Figure 3.3: Domain-mean potential temperature $<\theta>$ and mass mixing ratio $<r_T>$ profiles of the ensemble of LES simulations at four different times, from Brown et al. (2002). Thin black line represents the initial profile used during simulations.

3.3 General Cloud Development

The general cloud development is analysed through four different variables: total cloud fraction, maximum cloud fraction, cloud-base height and cloud-top height. Total cloud fraction is the maximum fraction of cloud in a given vertical column. Maximum cloud fraction is the maximum fraction of cloud over the entire domain. Results are shown in Figure 3.4a and compared to that found by Brown et al. (2002) in Figure 3.4b.

The first clouds form four hours into the simulation, shortly before 1600UTC. In comparison to the simulations run by Brown et al. (2002), this time of appearance is later than some of, but still within the spread of the models in Figure 3.4b, where clouds started to develop shortly after 1500UTC. There are three stages of cloud development: rapidly developing stage, mature stage, and decay stage. The rapidly developing stage is the period when total cloud fraction and cloud-top height are increasing quickly, they level off during the mature stage, and diminish during the decay stage. The clouds rapidly develop from approximately 1600UTC to 2000UTC, and are mature from 2000UTC to 2300UTC. Thereafter they decay until they disappear shortly after 0100UTC.

Total cloud fraction peaks during the mature stage. The maximum cloud fraction at a given level however peaks during the rapidly developing stage, before reducing gradually during the mature stage. However, the results from the LES models studied by Brown et al. (2002) show that the total cloud fraction peaks during the rapid development stage. MONC simulates a peak in total cloud fraction of over 30% at approximately 2100UTC. The majority of the simulations from the work by Brown et al. (2002) have a peak of total cloud fraction between 20% and 30%, occurring earlier at 1800UTC. The maximum cloud fraction at a given level simulated by MONC is somewhat lower in magnitude than some of the LES models, but is within the spread of results. The maximum cloud fraction peaks at the same time in both MONC and in the simulations run by Brown et al. (2002). The base of the clouds steadily increases throughout the day, from 700m-800m to approximately 1200m. The gradual rise of cloud-base corresponds to the increasing depth of the boundary layer. Cloud-top heights increase quickly during the developing stage, reaching a maximum height of approximately 2.7km, just above the capping inversion in the free troposphere during the mature stage. They reduce in height during the decay stage, eventually meeting with the increasing cloud-base. The depth and height of the cloud layer as simulated by MONC is in agreement with that found by Brown et al. (2002).

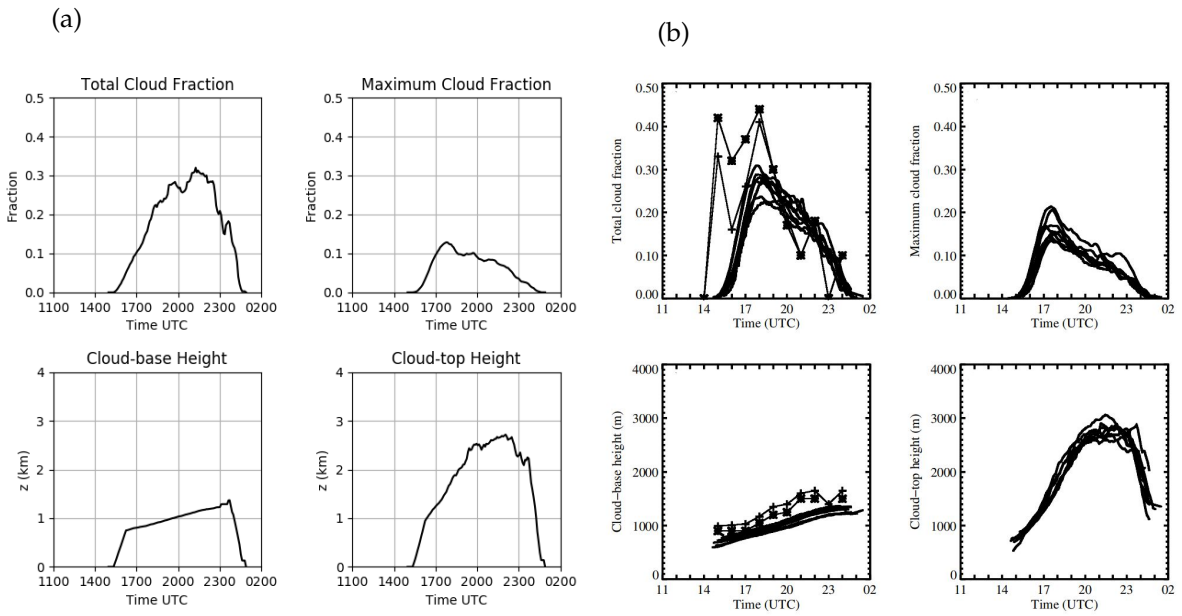

Figure 3.4: A comparison of the general evolution of clouds as simulated by (a) MONC, to that by (b) the ensemble of LES simulations from Brown et al. (2002). Starred points in Figure 3.4b correspond to observations taken at the ARM site.

3.4 Velocity Variance

The turbulent motion associated with shallow convection can be examined through wind velocity variance. The vertical profiles of horizontal velocity variance ($< u'u' >$) and vertical variance ($< w'w' >$) are considered, and compared to results from the other models examined by Brown et al. (2002). Profiles were chosen at two times, when there was no cloud present (1530UTC) and during the active phase of convection (2030UTC). In should be noted, that in Brown et al. (2002), an earlier time of 1430UTC was chosen. However the magnitudes for variance as simulated by MONC at this time both in the horizontal and vertical are too low to make a meaningful comparison, and so the later time of 1530UTC was chosen.

The profiles of variance before the formation of cloud in Figure 3.5 show the structure of dry boundary layer convection. Rising air from the surface results in a peak of $< w'w' >$ in the middle of the boundary layer. A near surface horizontal convergence also occurs, resulting in $< u'u' > \neq 0$ on or near the surface. The top of the boundary layer acts like a lid for this convective motion, where the air spreads horizontally, resulting in a peak of $< u'u' >$ and the diminishment of $< w'w' >$. Comparing Figures 3.5a & 3.5b pre-cloud formation, there is good agreement between the two. However the magnitude of $< u'u' >$ simulated by MONC is weaker than that in the models in Figure 3.5b. MONC simulates peak $< u'u' >$ at $0.2\text{m}^2\text{s}^{-2}$, weaker than that in the other models which has peak values of $< u'u' >$ spreading between $0.7\text{m}^2\text{s}^{-2}$ and $1.2\text{m}^2\text{s}^{-2}$.

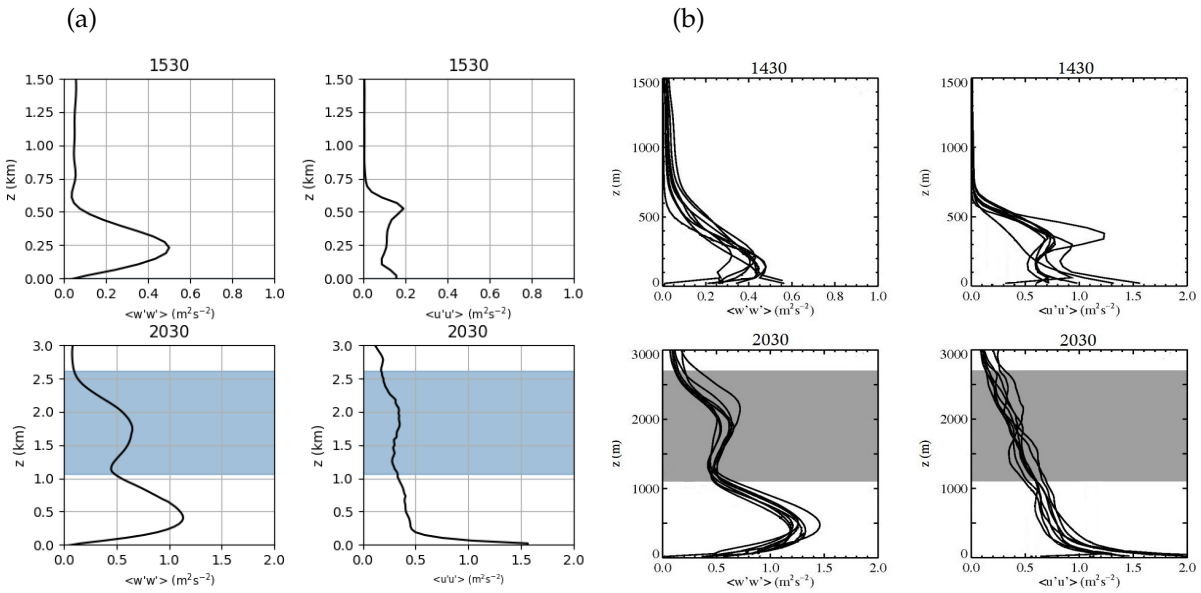

Figure 3.5: A comparison of the horizontal and vertical velocity variance as simulated by (a) MONC at times 1530UTC and 2030UTC, to (b) the LES ensemble from Brown et al. (2002) at times 1430UTC and 2030UTC. Shaded regions mark cloud depth.

After clouds form, the structures of the velocity variance changes due to different turbulent dynamics associated with cloud activity. As seen in the 2030UTC graph of Figure 3.5a, increased vertical motion within the clouds produces a second peak of $<w'w'>$. The motion in the subcloud layer is similar to that from the 1530UTC profile, with $<w'w'>$ peaking in the middle of the boundary layer. As there is increased vertical motion associated with the clouds, the top of the boundary layer no longer impedes vertical motion. The peak in $<u'u'>$ therefore is no longer present and instead $<u'u'>$ remains relatively constant with a small decrease with height. The results agree well with that found by Brown et al. (2002). The only discrepancy again being a weaker magnitude of $<u'u'>$ in the subcloud layer. From 250m to cloud-base, $<u'u'>$ is less than 0.5 m^2s^{-2}, while the LES results from Brown et al. (2002) all produce a stronger magnitude (>0.5m^2s^{-2}) in the subcloud layer.

3.5 Core Fraction and Mass Flux

As mentioned in Section 1, the categorisation of core points in diagnostics is often used when considering cloud dynamics. Core points within the simulation are defined as points that contain cloud with positive vertical velocity, and are positively buoyant with respect to the layer mean. Figure 3.6 shows the results for the fraction of core points and the mass flux of core points at two different times, 1830UTC and 2030UTC. These times correspond to when clouds are in the rapidly developing stage, and when the clouds are in the mature stage. In Figure

3.6a, both the core fraction and core mass flux as simulated by MONC peak near the cloud-base when clouds are in their development stage. Within the upper portion of cloud, there is little core activity. At the later time of 2030UTC, there is still a peak near cloud-base but the core fraction and mass flux decrease more linearly with height. In the mature stage, the cloud layer has increased buoyancy throughout the entire depth of cloud, as opposed to only being buoyant very close to cloud-base. This development is consistent to that determined by Brown et al. (2002). Although the MONC results are within the spread of results in Figure 3.6b, the magnitudes of core fraction and mass flux are lower than most of the models.

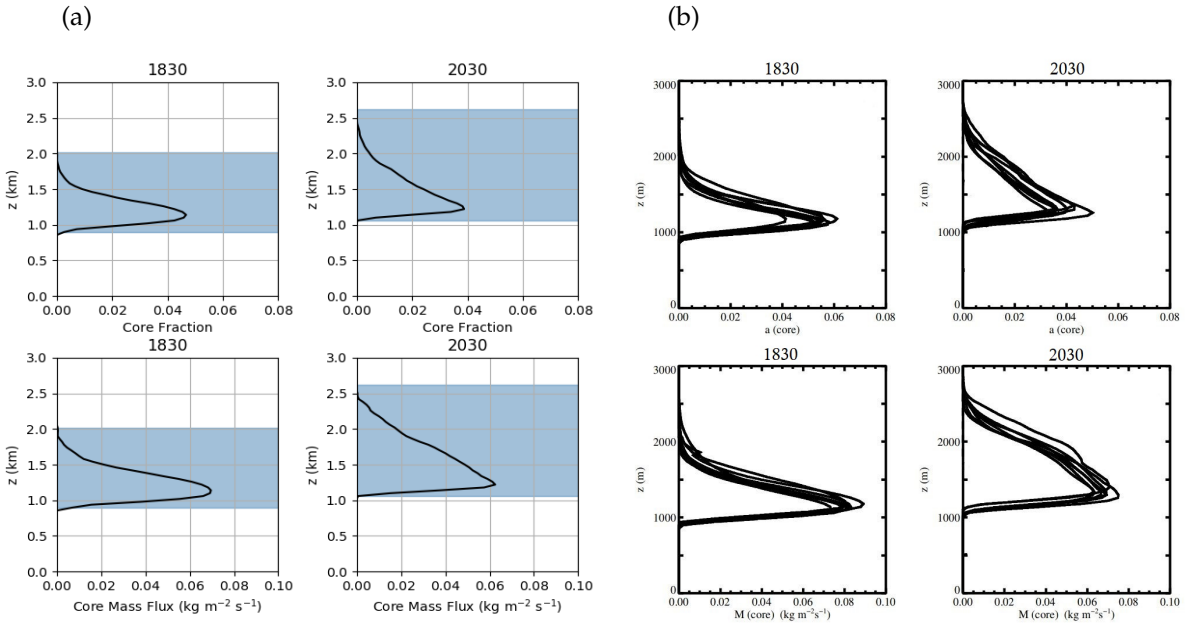

Figure 3.6: Comparison of core fraction and core mass flux as simulated by (a) MONC to (b) the LES ensemble studied by Brown et al. (2002). Shaded regions indicate cloud depth.

3.6 Discussion

This analysis of the control simulation suggests that the output from MONC is in agreement with the results from the other LES models as studied by Brown et al. (2002). Early in the simulation, dry convection develops in the clear boundary layer. The clouds start to develop 4 hours into the simulation and rapidly develop, with a depth of 1.5km during the mature stage, before dissipating after 2330UTC. The boundary layer depth grows steadily throughout the simulation period, as the model correctly simulates the mixing of air near the surface. The simulated moist convection shows the transport of moisture from the boundary layer into the free troposphere, and the corresponding drying of the boundary layer. The model successfully reproduces all stages of the life cycle of shallow convection. This includes the dry boundary layer convection before clouds form, the rapid development of clouds, the maturing of clouds

and the decay of clouds as surface forcing fades. Minor differences are observed between MONC results and those studied by Brown et al. (2002). These include the weaker magnitudes of $< u'u' >$ in the boundary layer and subcloud layer, and the delay in the peaking of total cloud fraction. The weaker magnitudes of $<u'u'>$ in the boundary layer in comparison to that of the models in Brown et al. (2002) may be because many of the models in Brown et al. (2002) have formed clouds earlier, and so convection developed at an earlier time. The majority of the results from this control simulation are very similar to that found by Brown et al. (2002). From the strong correlation with the results from Brown et al. (2002) it can be concluded that MONC can suitably simulate shallow convection over land. The model can therefore be used to investigate what controls the development of shallow convection, as described in the following section.

4 Sensitivity to Initial Humidity

In this section the sensitivity of shallow convection to initial humidity is investigated. The results of simulating shallow convection within environments of varying humidity levels are presented. The simulations are initialised with different initial mass mixing ratio profiles. Otherwise the model set up is as described for the control simulation. The control simulation has an initial surface relative humidity of 65%.

4.1 Initial Humidity Profiles

To examine model sensitivity to initial humidity, several simulations were run using varying initial humidity conditions. In doing this, new initial mass mixing ratio profiles are created. They correspond to $\pm$ 10% and $\pm$ 20% of the initial surface relative humidity used in the control simulation. The steps taken in formulating these new initial mixing ratio profiles are as follows. First, the initial surface relative humidity (RH) of the control simulation is determined using the following equation.

$$RH = \frac{r}{r_s} \tag{4.1}$$

Where "r" is the mass mixing ratio and "r_s" is the saturated mixing ratio. This initial saturated mixing ratio is determined using the initial pressure and temperature at the surface, which are known.

$$r_s = \frac{R_d}{R_v}\frac{e}{e_s - P} \tag{4.2}$$

Where "e_s" is the saturated vapour pressure, and is calculated using the following equation.

$$e_s(T) = e_s(T_0)e^{\frac{L_v}{R_v}\frac{1}{T_0}-\frac{1}{T}} \tag{4.3}$$

The standard values of $e_s(T_o)$ = 611Pa at T_0 = 273.15K are chosen. The constants R_d, R_v and L_v are the specific gas constant for dry air, the specific gas constant for water vapour, and the latent heat of vaporization, respectively. Using this method, the surface RH of the control simulation is calculated to be approximately 65%. The new initial humidity profiles therefore have an initial surface RH of 45%, 55%, 75% and 85%.

Next, the new initial mass mixing ratio profiles ($<r_T>$) are determined that correspond to the new surface RH values. To prevent any negative RH values at higher levels, the new $<r_T>$ profiles were unperturbed for model levels above 2.5km. The new initial $<r_T>$ profiles and corresponding relative humidity profiles are shown in Figure 4.1. The model configuration file is updated with the new initial $<r_T>$ profile. This produces an ensemble of four simulations that differ only by the initial $<r_T>$ curve. The analysis of these different outputs, and comparison to the control simulation are given below. The simulations are named SIM45, SIM55, SIM75 and SIM85 which correspond to the simulation with an initial surface RH of 45%, 55%, 75% and 85%, respectively.

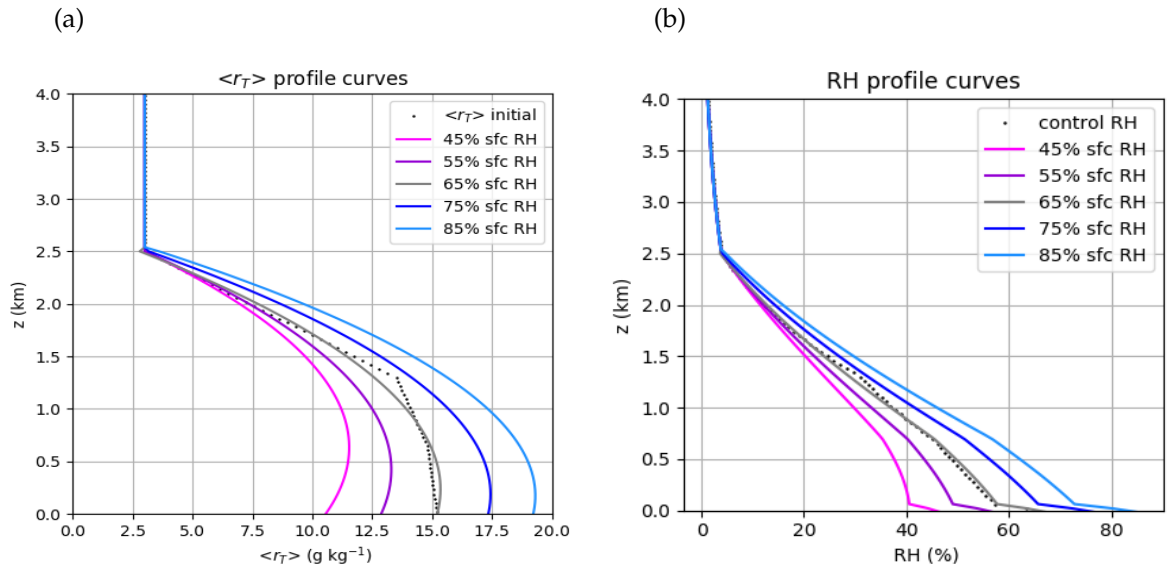

Figure 4.1: Vertical profiles of (a) the new $<r_T>$ initial conditions and (b) corresponding initial relative humidity conditions. The initial profile used in the control simulation is shown as the black dotted line and the grey line represents the corresponding line of best fit.

4.2 Evolution of Mean Potential Temperature and Mixing Ratio

Figure 4.2 compares the evolution of the thermodynamic profiles between all the of simulations. Focusing on the top panel of Figure 4.2, some spread occurs between the mean potential temperature profiles in the free troposphere at the end of the period. At 2030UTC and 2330UTC, the most unstable potential temperature profiles are in SIM75 and SIM85. By 2330UTC, there is a difference of over 3K in the potential temperature at 3km between SIM45 and SIM85. Therefore, an increase in initial humidity increases free tropospheric instability. SIM45 and SIM55 have almost the exact same lapse rate as each other, being slightly more stably stratified than the control simulation. At 2330UTC, the height of the capping inversion is a function of increasing initial humidity, found at approximately 3.3km in SIM85, in comparison to a height of

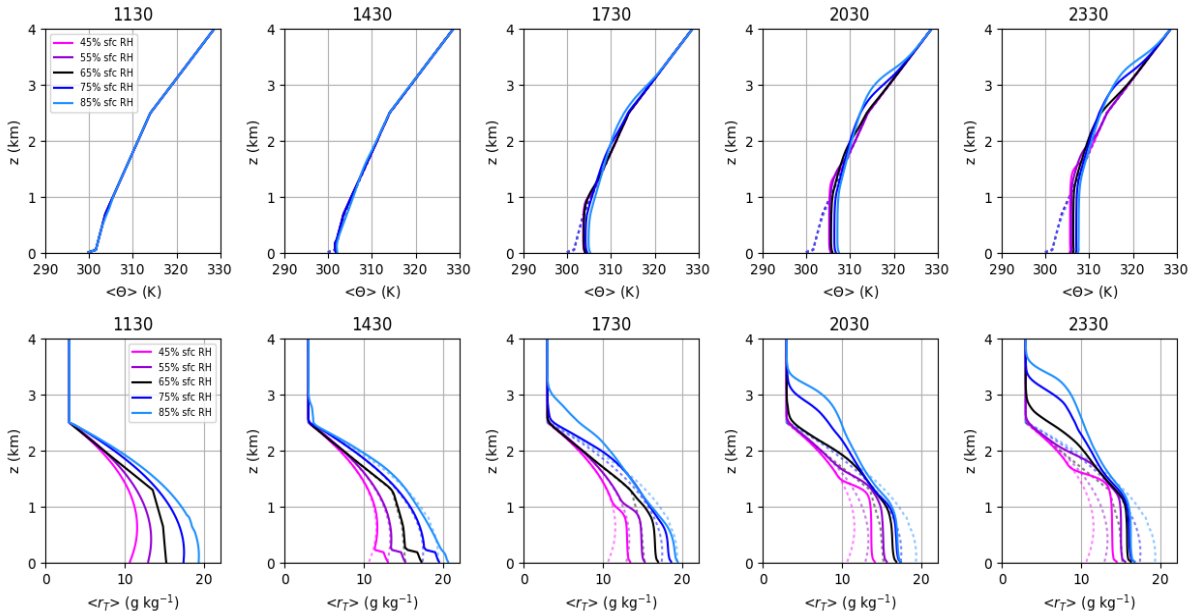

Figure 4.2: Domain-mean potential temperature and mass mixing ratio profiles for the simulations. Results are shown at five different times. Dashed lines represent the initial profiles used during simulations. Pink, purple, navy and blue lines correspond to SIM45, SIM55, SIM75 and SIM85, respectively. The black line represents the control simulation data.

2.5km for SIM45 and SIM55. In contrast, the depth of the boundary layer is a function of decreasing initial humidity. The top of the boundary layer reaches a height of 1400m for SIM45 at 2330UTC, however in SIM85, the top of the boundary layer has reached approximately 1000m by this time. In other words, the boundary layer depth grows at a quicker rate for simulations with the lower initial moisture content. All simulations started with the same initial potential temperature profile, although the boundary layer increases in temperature at a faster rate for simulations with higher initial humidity. By 2330UTC, the mean boundary layer potential temperature is approximately 2K higher for SIM85, than for SIM45.

The lower panel of Figure 4.2 shows how the mean moisture content evolves throughout the day. As in the control simulation, the increasing surface latent heat flux allows the development of boundary layer moisture content, seen to occur from 1430UTC. All simulations experience an increase of moisture near the surface by 1430UTC, and by 1730UTC the boundary layer has uniformly moistened. SIM75 and SIM85 experience the lowest increase in boundary layer moisture and at 1730UTC the boundary layer of these simulations starts to dry as the free troposphere correspondingly gains moisture. This moisture gain of the free troposphere is significant, with SIM75 and SIM85 having 3.5gkg^{-1} and 5.7gkg^{-1} more moisture respectively than all the other simulations at 3km by 2330UTC. In contrast, SIM45 and SIM55 encounter little to no moistening of the free troposphere throughout the simulation. Therefore, by 2330UTC, the spread of moisture content in the free troposphere is much greater between all the simulations

than that in the boundary layer. Higher amounts of moisture are being transported to deeper depths into the troposphere for a more initially humid environment.

4.3 General Cloud Development

Figure 4.3 shows the cloud evolution throughout the simulations. The general trend of a rapidly growing stage followed by a mature and then a decaying stage is present in all of the simulations. Clouds decay in all of the simulations at the same time, in synchrony with the decreasing surface forcing. The time at which cloud starts to develop varies between the simulations. A decrease in initial surface relative humidity by 10% delays the time of cloud production by 1 to 3 hours. Cloud growth rate is increased for simulations with higher initial humidity conditions.

As seen in Figure 4.3, the total cloud fraction during the mature stage of cloud development is dependent on initial atmospheric humidity. The total cloud fraction increases by approximately 7% per 10% increase in initial surface relative humidity above 65%. The total cloud fraction reduces by approximately 15% per 10% decrease in initial surface relative humidity below 65%. In SIM85, high cloud fraction occurs very early during the simulation from 1200UTC onwards, with cloud covering the entire domain very near the surface and at a depth of approximately 400m-700m during the period between 1200UTC to 1230UTC. Although the maximum cloud fraction reduces to more expected levels by 1430UTC, the total cloud fraction continues to increase. In SIM85, the clouds are developing rapidly from 1200UTC, and are already quite mature by 1630UTC, before some of the other simulations had even produced cloud. Similarly, SIM75 experiences an anomalously large maximum cloud fraction of 40% from 1200UTC to 1230UTC. Cloud-base and cloud-top height remain close to zero during this period. After this period, cloud fraction returns to zero and by 1430UTC boundary layer cloud starts to develop, reaching maturity by approximately 1730UTC. The anomalously high values for maximum cloud fraction occurring near the surface early in SIM85 and SIM75 is thought to be fog, as it clears away by 1230UTC, when the surface sensible heat flux becomes positive.

Initial humidity does not have a large impact on the cloud-base height, as all of the simulations follow the same pattern of a cloud-base rising as boundary layer depth grows. A sudden increase in cloud-base is seen at approximately 2300UTC for SIM85. Unlike cloud-base height, the spread in cloud-top height between the simulations throughout the period is significant. The peak cloud-top height increases by approximately 500m with a 10% increase in initial surface humidity. When mature, the clouds produced in SIM85 reach heights of over 3.5km, while in comparison SIM45 has a cloud-top height of 1500m. The entire cloud layer depth of SIM45 is approximately 200m throughout the entire simulation, with less than 5% cloud fraction.

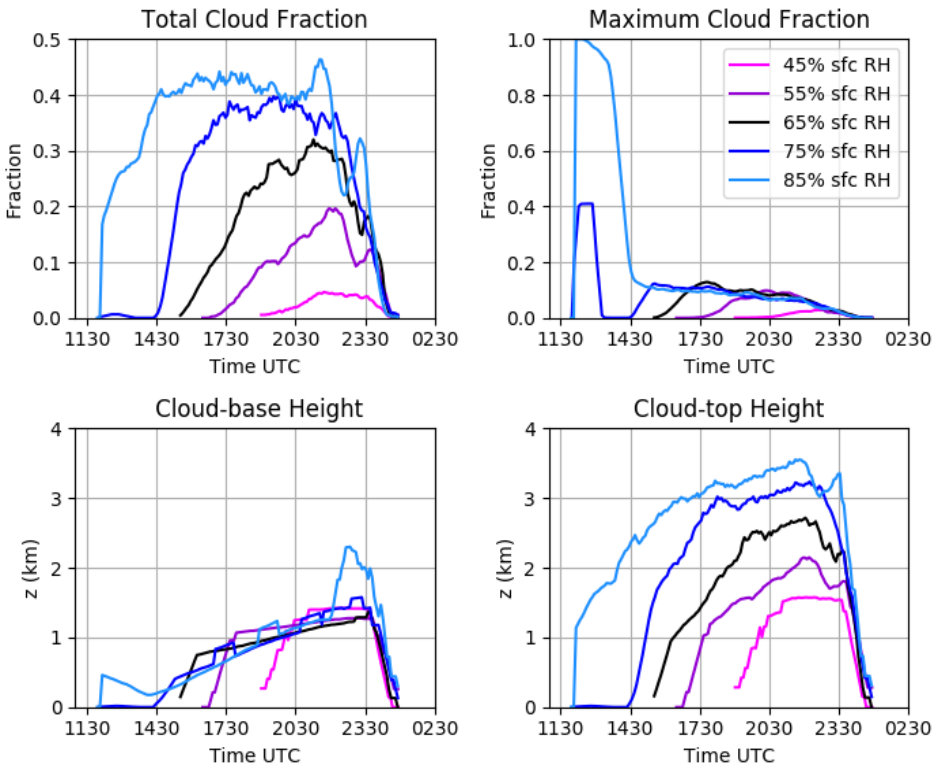

Figure 4.3: The evolution of clouds in the simulations with varying initial humidity profiles. Pink, purple, navy, and blue lines correspond to SIM45, SIM55, SIM75 and SIM85, respectively. The black line represents the control simulation data.

To highlight the significant spread in cloud fraction between the simulations, a time-height cross section of cloud fraction is shown in Figure 4.4. The initial production of surface condensation mentioned previously in SIM75 and SIM85 is seen. For all initial humidity conditions, the highest cloud fraction occurs at the cloud-base, particularly during the rapid development stage. There is a sudden reduction in cloud fraction throughout the majority of the cloud layer in SIM85 at approximately 2300UTC. This corresponds to the sudden rise in cloud-base and a reduction in cloud height for this simulation at this time seen in Figure 4.3.

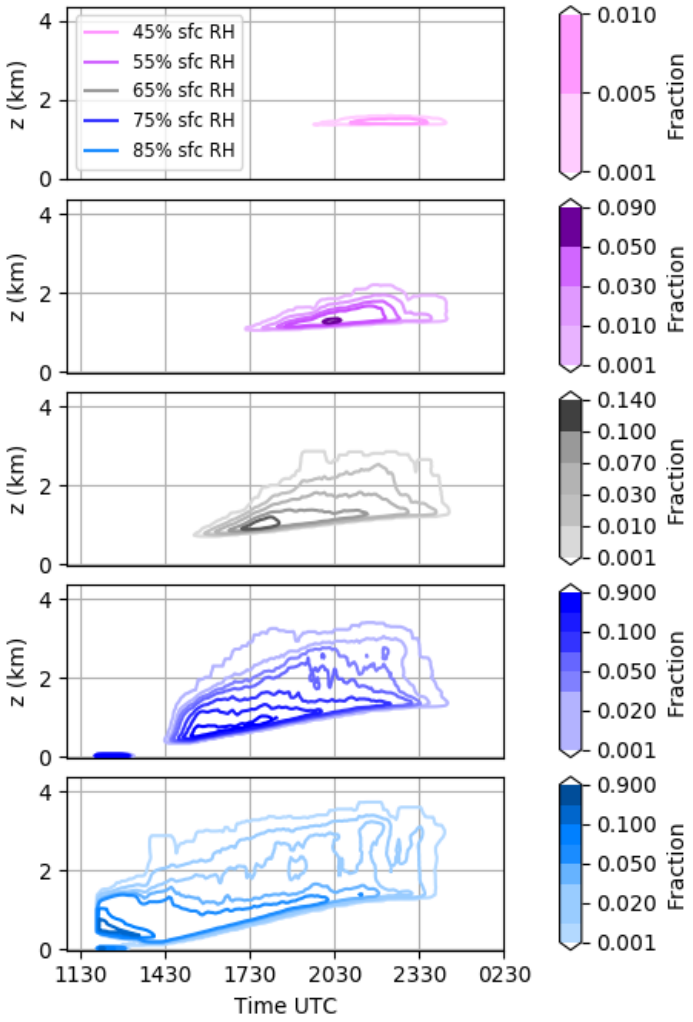

Figure 4.4: Time-height cross section of cloud fraction in the various simulations. Pink, purple, navy, and blue lines correspond to SIM45, SIM55, SIM75 and SIM85, respectively. The grey lines represent the control simulation data.

Although precipitation is not present in the control simulation, it may still be feature in some simulations. A time series of surface precipitation is shown in Figure 4.5. Precipitation is negligible in all simulations but there is light precipitation in SIM75 and SIM85. There was a small amount of precipitation which fell at a consistent rate during the period at which fog was present. This may be drizzle associated with the fog. Two other periods with a brief, sharp increase in precipitation occur during SIM85 at 1445UTC and over seven hours later just before 2200UTC. After the 1445UTC precipitation event, cloud-top height reduces and the base starts to increase. The precipitation event just before 2200UTC coincides with the sudden reduction in cloud fraction and sudden increase in cloud-base which occurs thereafter, as mentioned previously. The location of surface precipitation over the horizontal domain during these three precipitation events is also shown in Figure 4.5. Total cloud fraction is shown in grey. At

1200UTC, very light cloud and precipitation is uniform across the entire area. This confirms that the light drizzle and high maximum cloud fraction is associated with fog. The two other heavier precipitation events at 1445UTC and 2150UTC can be seen as isolated showers of higher rainfall in the domain.

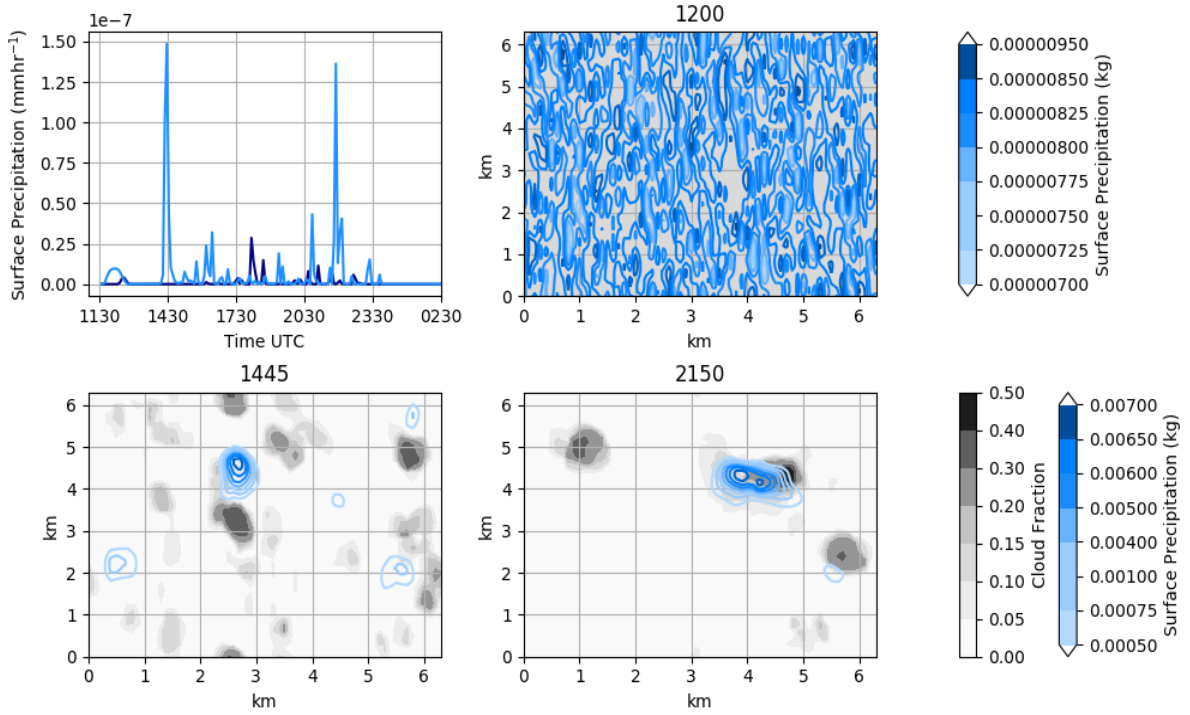

Figure 4.5: A time series of the total domain precipitation in SIM75 and SIM85 is represented by blue and navy lines, respectively. Surface precipitation (blue) and total cloud fraction (grey) are shown for SIM85 during the precipitation events at 1200UTC, 1445UTC and 2150UTC.

Another method of comparing the cloud development between the different simulations is to consider the liquid water path (LWP) of each simulation. The time series of the LWP is shown in Figure 4.6. The LWP of SIM45 is negligible. the LWP in all of the simulations generally increases as the clouds are developing, before leveling off as the clouds are maturing, and finally decreases accordingly with cloud decay and the reduction in surface forcing. It is clear that LWP increases with increasing initial humidity. The sharp drop in LWP in SIM85 at approximately 1330UTC occurs after the fog clears. A small amount of LWP in SIM75 is also seen before this time. Following another strong peak, the LWP of SIM85 reduces sharply again after 1430UTC, coinciding with the 1445UTC precipitation event. A third and final sharp drop in LWP for this simulation occurs shortly after 2200UTC, following the 2150UTC precipitation event.

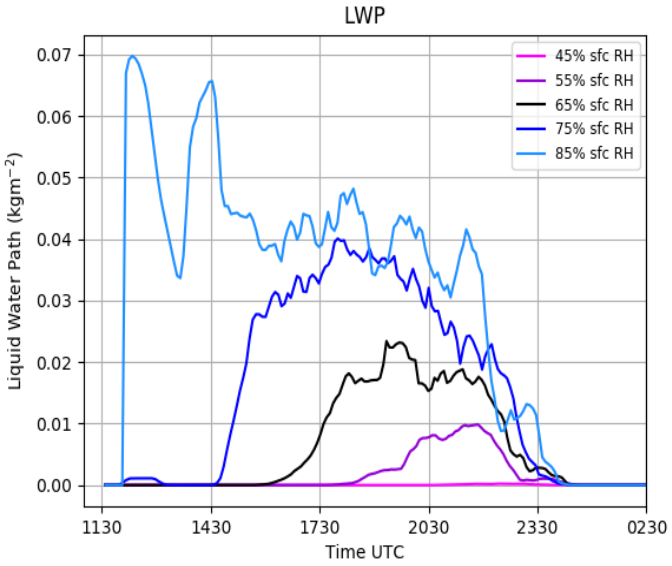

Figure 4.6: A time series of the liquid water path of the simulations. Pink, purple, navy, and blue lines correspond to SIM45, SIM55, SIM75 and SIM85, respectively. The black line represents the control simulation data.

4.4 Velocity Variance

The horizontal and vertical velocity variance of the simulations are compared in Figure 4.7. Ideally, the two times at which variance is examined should correspond to a time when no cloud was present in the simulations, and a later time during the active phase of convection. However, there was no time of which all the simulations had no cloud, as SIM75 and SIM85 produced cloud early during the simulation. The times chosen were 1530UTC and 2130UTC, and in general the comparison is made between the simulations with cloud formed, or without cloud present.

At 1530UTC, no cloud has formed in SIM45, SIM55 and the control simulation. The clear boundary layer structure of $<u'u'>$ with a peak present at the top of boundary layer is identical between these simulations, as seen in Figure 4.7a. There is no significant change in magnitude as a result of different initial humidity before clouds form. SIM75 and SIM85 have cloud formed at this time. The distinctive boundary layer peak in $<u'u'>$ is no longer present, and there is an increase of variance throughout the cloud layer. This structure is consistent with that at 2130UTC, when the convection is more active. At 2130UTC, the magnitude of $<u'u'>$ has increased in all of the simulations. SIM45 has the least similar profile to all the simulations at this time. It has very minimal amount of cloud and the variance diminishes significantly in the free troposphere. In SIM75 and SIM85, the cloud layer is over 2km deep, and $<u'u'>$ has developed a peak at cloud-top. This is likely due to increased horizontal spreading as rising air reaches the capping inversion.

In Figure 4.7b, the vertical velocity variance between the simulations is compared. Again, at 1530UTC, the simulations with no cloud formed all have very similar profiles of $<w'w'>$. The structure in $<w'w'>$ changes as soon as cloud is present. The secondary peak of $<w'w'>$ associated with cloud activity has already developed by 1530UTC in SIM75 and SIM85. The magnitude of $<w'w'>$ in the subcloud layer however is very low at this time. At 2130UTC when the clouds are in their mature stage, the magnitude of the $<w'w'>$ in the cloud layer increases by approximately $0.025 m^2 s^{-2}$ for a 10% increase in initial surface humidity. For SIM45, there is very little cloud, and $<w'w'>$ is negligible in the cloud layer. In contrast, the boundary layer peak is significant for this simulation. This peak of variance in the boundary layer decreases with increasing initial humidity, although the change in magnitude with initial humidity is less significant than that in the cloud layer.

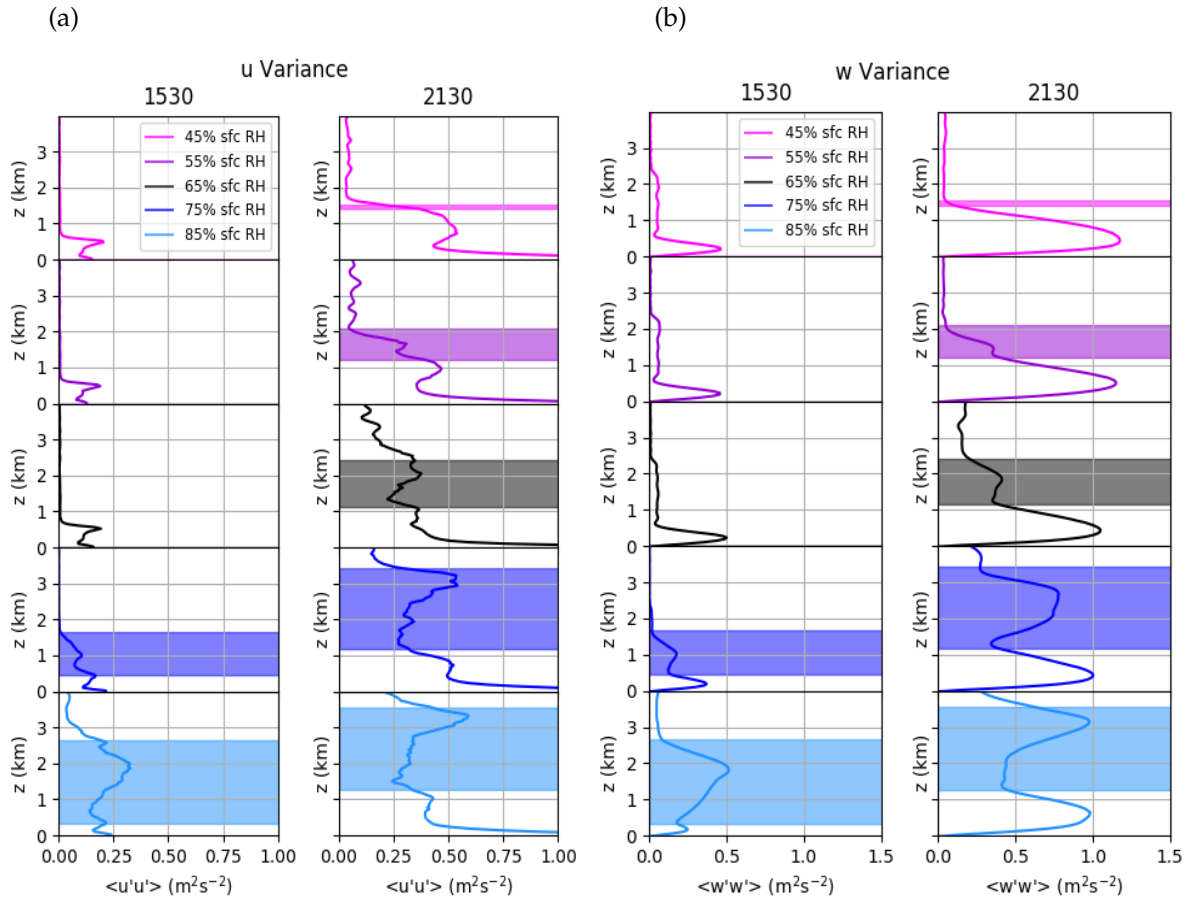

Figure 4.7: The (a) horizontal and (b) vertical velocity variance at two times, 1530UTC and 2130UTC. Pink, purple, navy and blue lines correspond to SIM45, SIM55, SIM75 and SIM85, respectively. The black line represents the control simulation data. Shaded regions correspond to depth of cloud layer at that time.

4.5 Core Fraction and Mass Flux

The simulations are compared in terms of the core fraction and core mass flux. The comparison should be made when the convection is in the rapidly developing stage, and in the mature stage. As this occurs across various times for the different simulations, three times during the simulation period are chosen in an attempt to capture all of the simulations in both of these stages. The times chosen are 1830UTC, 2030UTC, and 2130UTC, and results are shown in Figure 4.8.

Core fraction is shown in Figure 4.8a. SIM45 has no core points. SIM55 has a delayed development of core points with respect to the control simulation. The cloud core fraction characteristic of the rapidly developing stage, only appears from 2030UTC for this simulation. The cloud development has matured slightly more by 2130UTC, and the peak reduces. In contrast, SIM75 is already quite mature by 1830UTC and has a larger depth of buoyant cloud than that of the control simulation for this time. As the convection continues to mature, the peak of core fraction softens from 2030UTC onwards. Similar structure is seen in the core fraction of SIM85. The development of a higher fraction of buoyant cloud layer is therefore enhanced for runs with initially moisture conditions.

The same result is found for the core mass flux, shown in Figure 4.8b. Core mass flux is higher for initially more humid simulations and development of profiles occurs at a faster rate. The core mass flux profile for SIM55 at 2130UTC is that of the control simulation three hours earlier. At 1830UTC, SIM75 and SIM85 have developed a secondary peak in mass flux in the middle of the cloud layer, in addition to the expected peak at cloud-base. This secondary peak is a sign that the cloud layers are more actively convective than that of the control run at this time. Overall, the buoyancy increases with increased initial humidity. An initial surface relative humidity of at least 55% is required for the production of buoyant cloudy parcels. An initially more moist atmosphere results in the advancement of the development of buoyant parcels, which initially are centered at cloud-base, and increase throughout the entire cloud layer. An environment with a initial surface relative humidity of at least 75% will produce a cloud layer that has a peak in mass flux of buoyant air in the middle of the cloud layer when clouds are mature. Initially drier atmospheres will produce a cloud layer with a peak in mass flux solely near the cloud-base.

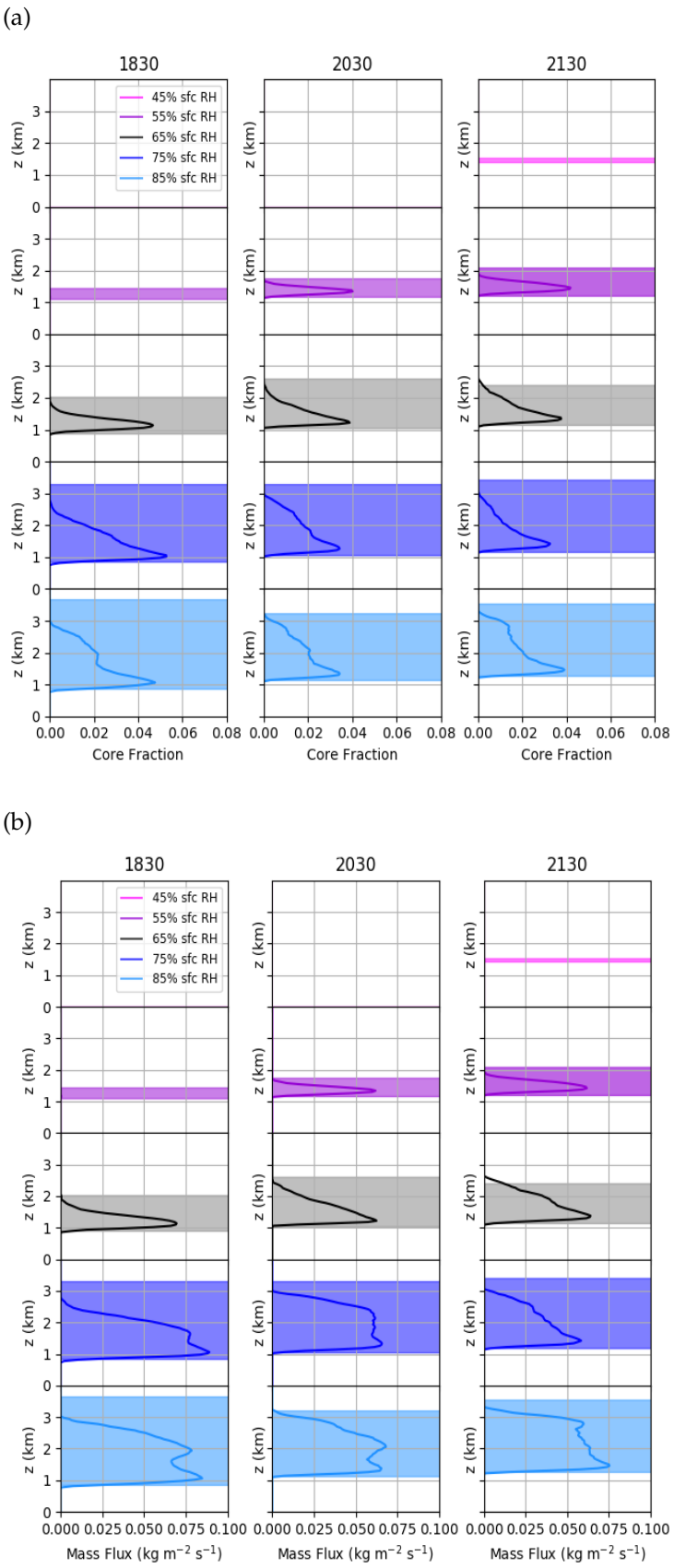

Figure 4.8: (a) Core fraction and (b) core mass flux shown at three times of 1830UTC, 2030UTC and 2130UTC. Pink, purple, navy and blue lines correspond to SIM45, SIM55, SIM75 and SIM85, respectively. The black line represents the control simulation data. Shaded regions mark cloud depth at that time.

4.6 Discussion

The evolution of shallow convection is clearly impacted by the initial atmospheric moisture content. An initially moister atmosphere acts to de-stabilise the free troposphere, resulting in an increase in the height of the capping inversion. This allows the enhancement of cloud-top height and the earlier production of clouds for initially moister conditions. The increase in cloud amount for initially moister simulations occurs as there is increased transport of moisture from the boundary layer into the free troposphere. The boundary layer of the environments with initially higher moisture content will dry earlier, significantly increasing free tropospheric moisture levels in comparison to those with less moist initial conditions. This finding is consistent with what was discussed in the literature, that moist updrafts associated with shallow convection transport moisture from the boundary layer into higher levels, subsequently moistening the free troposphere (Von Salzen et al., 2005). Drier initial conditions however hinder this transport, and instead result in higher boundary layer moisture content, with no moistening of the free troposphere. Therefore it seems that shallow convection can only transport moisture from the boundary layer into the free troposphere if the initial atmosphere is sufficiently moist.

Lower initial moisture levels also increase mixing in the boundary layer allowing it to grow deeper throughout the day than that of moister initial conditions. Even after clouds form, the subcloud layer velocity variance is highest for initially drier simulations. This indicates that boundary layer convection is stronger for initially drier simulations. The diminishing velocity variance profiles above the boundary layer is further evidence of the confinement of shallow convection within the boundary layer for drier initial conditions. When the atmosphere is more moist however, moist convection extends beyond the boundary layer and the enhanced cloud development amplifies cloud buoyancy and ascent.

The phase of the diurnal cycle of moist shallow convection also depends on the initial humidity conditions. A reduction of just $2 \mathrm{gkg}^{-1}$ of moisture at the surface delays the beginning of cloud production by several hours. The production of cloud within the model is very sensitive to an increase in initial moisture. The model responds to high initial relative humidity levels (of 75% and higher at the surface) with anomalously high yields of cloud fraction within metres of the surface. This condensation is thought to be fog, as it decays as the surface heating flux becomes positive. Light precipitation can be produced for an initially moister environment. Precipitation only occurs when the initial surface relative humidity is at least 65%. Other than light drizzle associated with fog early in the morning, precipitation also falls as isolated light showers later in the day. Cloud fraction and LWP are reduced significantly after a precipitation event.

The impact of initial humidity on cloud-top height is significant, and the depth of the cloud layer is very sensitive to initial humidity conditions. The cloud-base will be lower in conditions that are moister. It is thought that the decrease in free tropospheric stability and increased

height of capping inversion that occurs for higher initial humidity are responsible for the increase in cloud-top height with increasing initial moisture. The initial humidity condition does not affect the stages of growth, as all the humidity conditions produced convection cycles with a developing, a mature and a decaying stage. Initial humidity does however have a large impact on the total cloud fraction in a column, although maximum cloud fraction at a given height was less affected. A higher moisture content will encourage cloud development. The general evolution of highest cloud fraction at cloud-base during the developing stage, followed by gradual increase in fraction through cloud layer, is not affected by initial humidity.

The profiles of horizontal and vertical velocity variance emphasise that the convection occurring in the boundary layer and subcloud layer is much stronger for initially drier atmospheres. An increase in initial atmospheric moisture will increase the vertical transport of mass and moisture associated with moist convection. Fraction of core points and core mass flux will also increase with an increase in initial humidity. For cloudy air parcels to be buoyant, a surface initial humidity of over 45% is required. The number of buoyant air parcels will increase with an increase in initial humidity. The increased core mass flux and development of a second peak in the cloud layer indicate that the initial atmospheric humidity fuels in-cloud convection. The increase in vertical variance in the cloud, and the evidence of horizontal spreading at the capping inversion in the initially moister simulations further add to this picture of enhanced convective activity within the cloud.

These results allow a quantitative description of the impact of humidity on the life cycle of shallow convection over land. The general structures of the profiles of the various variables described in the control simulation are maintained in these sensitivity simulations. Largest impacts of initial humidity conditions are on the rate of cloud development, free tropospheric moisture content, cloud-top height and total cloud fraction. The findings are consistent with previous study by Derbyshire et al. (2004), which concluded that a deepening of convection occurs for more humid mid-troposphere, and drier environments result in a shallowing of deep convection. The results from this dissertation show that this is also true for shallow convection.

5 Sensitivity to Initial Stability

This section gives the analysis and discussion of the results which investigate the sensitivity of shallow convection to initial atmospheric stability. The impact of the initial potential temperature of the environment on the development of clouds is explored. The simulations are divided into two categories, those with varying initial boundary layer stability, and those with varying initial free tropospheric stability.

5.1 Initial Potential Temperature Profiles

To understand the impact of atmospheric stability on the evolution and development of shallow convection, simulations are run with new initial potential temperature profiles. These are done under two regimes. Firstly by varying the initial potential temperature profile in the boundary layer, and secondly by varying the initial potential temperature profile in the free troposphere.

To determine new boundary layer potential temperature profiles, the temperature inversion at the surface is removed. Without this surface inversion, the surface temperature in the control simulation increases from 299.5K to 301.3K. New potential temperature profiles are constructed by perturbing the surface potential temperature by $\pm$ 1K and $\pm$2K. For model levels above 700m, the potential temperature is left unchanged from the control simulation. Linear interpolation is used to construct a new $<\theta>$ profile from the various new surface temperatures, up to 700m. These new potential temperature profiles are shown in Figure 5.1a. The varying boundary layer potential temperature profiles are distinguished by their surface temperature. SIM299 and SIM300 refer to the simulations with an initial surface temperature of 299.3K and 300.3K respectively. These simulations with initially cooler boundary layers correspond to a more initially stably stratified environment than the control simulation. The simulation SIM301 refers to the simulation with an initial surface potential temperature of 301.3K. Other than the removal of the surface inversion, SIM301 has the same initial stability as used in the control simulation. SIM302 and SIM303 refer to the simulations with initial surface temperatures of 302.3K and 303.3K respectively. These simulations have an initially warmer boundary layer corresponding to an initially more unstable environment.

The new free tropospheric potential temperature profiles are chosen by leaving the original control simulation $<\theta>$ profile unchanged from the surface up to 700m. The potential temperature is increased by 2K and decreased by 3K at model levels above 2.5km. Linear interpolation is used to determine the new $<\theta>$ profiles from 700m to 2.5km. All profiles are capped with a temperature inversion at 2.5km and have identical lapse rates from 2.5km. The profiles of the new initial potential temperature conditions are shown in Figure 5.1b. FTM3 refers to the simulation with potential temperature reduced by 3K in the free troposphere. This simulation corresponds to an initially less stable environment. FTP2 refers to the simulation with potential temperature increased by 2K in the free troposphere. This simulation initially has a more stably stratified free troposphere corresponding to an initially more stable environment. Simulations are run with these new $<\theta>$ profiles, with all other parameters and initial conditions unchanged from the control simulation. Analysis and discussion of results of the sensitivity of the shallow convection to initial atmospheric stability are given below.

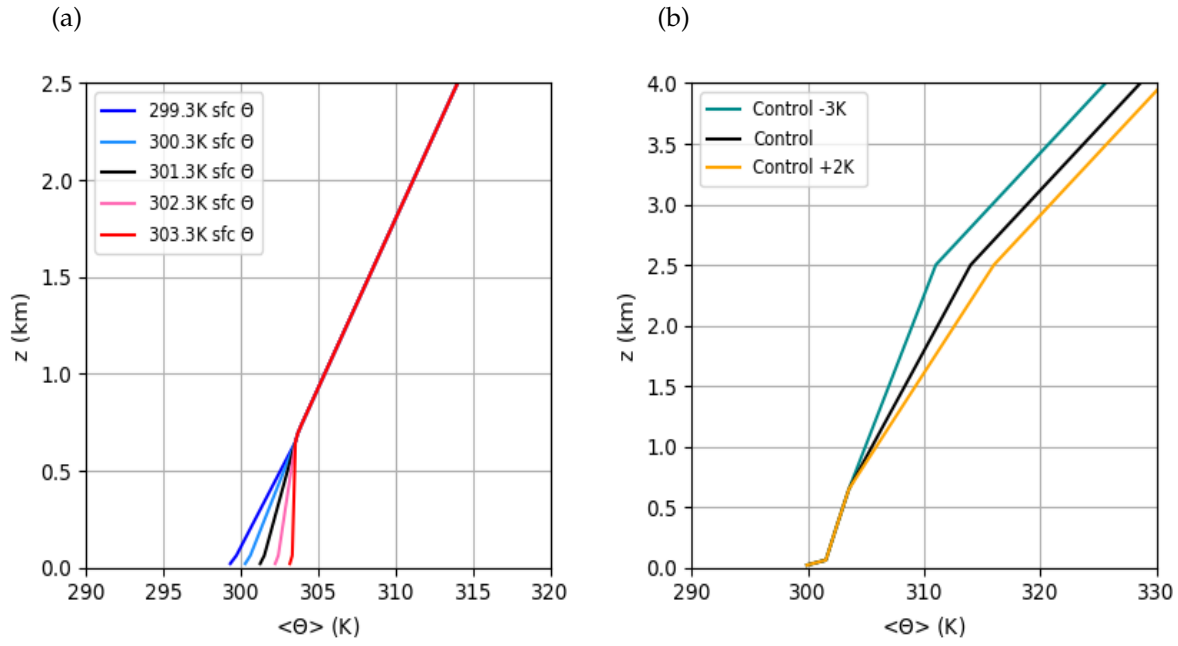

Figure 5.1: Vertical profiles of the new initial potential temperature conditions with a cooling and warming of (a) the boundary layer and (b) the free troposphere. In (a), navy, blue, black, pink and red lines correspond to SIM299, SIM300, SIM301, SIM302, and SIM303 respectively. In (b) the green, black and yellow lines correspond to FTM3, the control simulation and FTP2, respectively.

5.2 Evolution of Mean Potential Temperature and Mixing Ratio

The evolution of potential temperature in the simulations with varying initial boundary layer stability is shown in the top panel of Figure 5.2. The navy and blue lines correspond to simulations SIM299 and SIM300 respectively, and are more initially stably stratified. The pink and red

lines correspond to simulations SIM302 and SIM303 respectively and are initially less stable. The growth of boundary layer depth occurs steadily in all simulations throughout the simulation period. SIM299 and SIM300 experience a boundary layer warming greater than that of SIM302 and SIM303. By 2030UTC, the spread in surface temperature between all the simulations is less than it was initially at 1130UTC. SIM299 and SIM300 have a boundary layer depth that is slightly greater than that of SIM302 and SIM303. By 1130UTC, the boundary layer of SIM303 has reached a height of approximately 1400m, 200m greater than that of SIM299. All of the simulations evolve in the same manner in the free troposphere, indicating that the cloud-top height is not sensitive to the boundary layer stability. Above the boundary layer, they have seemingly identical potential temperature profiles throughout the simulation period. The development of $<r_T>$ between the simulations with varying boundary layer stability is shown in the lower panel of Figure 5.2. After the first three hours at 1430UTC, SIM302 and SIM303 experience a uniform increase of moisture throughout the boundary layer. However, like the control simulation, SIM299 and SIM300 experience a sharp increase in moisture near the surface. By 2330UTC, SIM299 and SIM300 have the highest boundary layer moisture content. However, at this time SIM302 and SIM303 have slightly higher free tropospheric moisture. In general, the spread of free tropospheric moisture content between all the simulations is otherwise insignificant.

The evolution of $<\theta>$ for varying free tropospheric stability is shown in the top panel of Figure 5.3. The green line corresponds to FTM3, and is initially more unstable. The yellow line corresponds to a FTP2, and is initially more stably stratified. In contrast to Figure 5.2, the potential temperature of the boundary layer grows identically in all the simulations. As expected, spread in $<\theta>$ between the simulations occurs in the free troposphere. By 2330UTC, all simulations experience a decrease in tropospheric stability, although at different heights. The potential temperature in FTM3 decreases between 2.5km-3.5km, with a sharper capping inversion at approximately 3.2km. FTP2 experiences a decrease in potential temperature between the boundary layer and 2.3km. Unlike that in Figure 5.2, the increase in boundary layer moisture is identical between the three simulations for the first six hours of the period. After this, the free troposphere begins to moisten. By 2330UTC, FTM3 significantly increases in moisture by up to 4gkg^{-1} between 2km-3.5km and boundary layer moisture correspondingly decreases. The boundary layer moisture content reduces to 14gkg^{-1}, drier than its initial value. FTP2 experiences little to no drying of the boundary layer by this time, and a lesser free tropospheric moistening than in the control simulation.

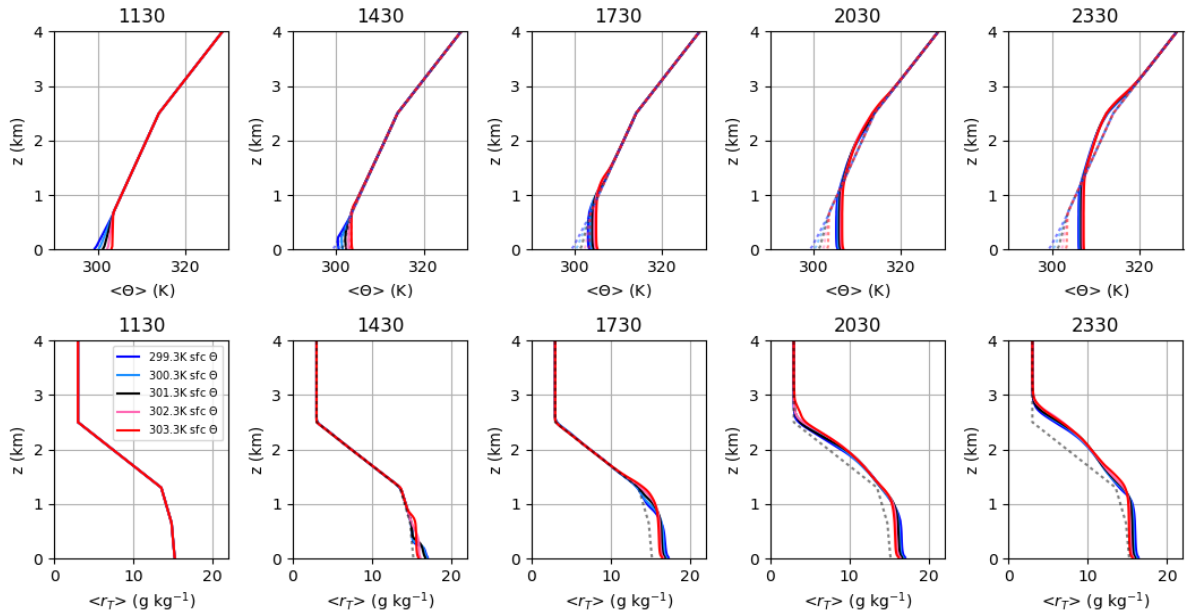

Figure 5.2: Domain-mean potential temperature and mass mixing ratio profiles for varying initial stability profiles in the boundary layer. Results are shown at five different times. Navy, blue, black, pink and red lines correspond to SIM299, SIM300, SIM301, SIM302, and SIM303 respectively. Dashed lines represent the initial profiles used during simulations.

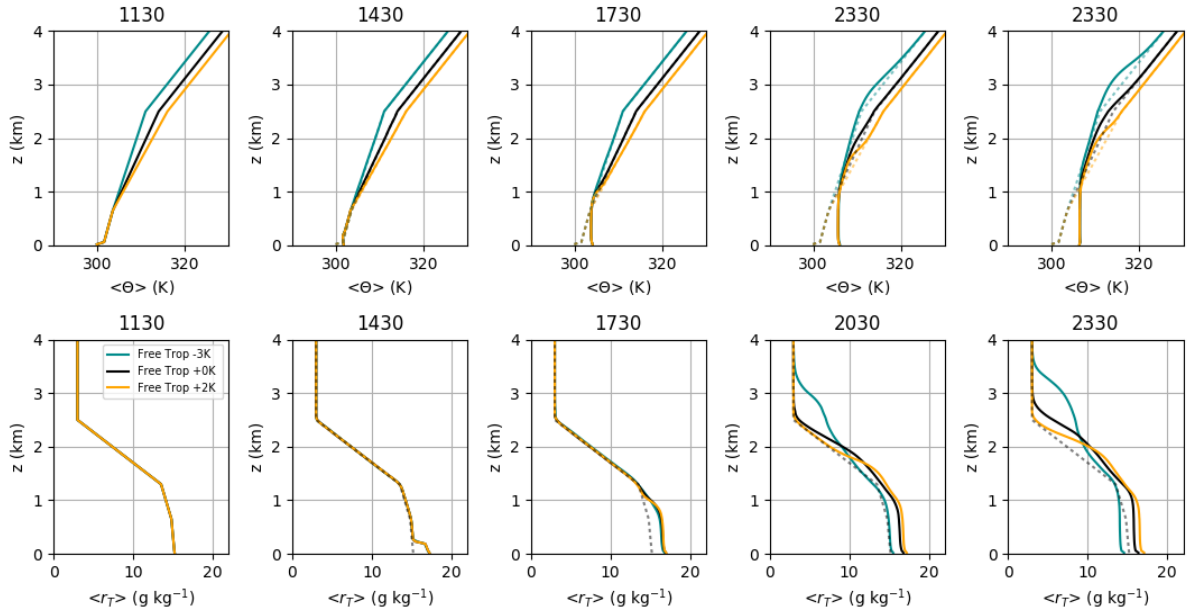

Figure 5.3: Domain-mean potential temperature and mass mixing ratio profiles for varying initial stability profiles in the free troposphere. Results are shown at five different times. Green, black and yellow lines correspond to FTM3, the control simulation and FTP2 respectively. Dashed lines represent the initial profiles used during simulations.

5.3 General Cloud Development

Figures 5.4 & 5.5 show the development of cloud fraction, cloud-base and cloud-top height. As before, the three distinct stages of cloud development can be seen in all of the simulations. Focusing on the evolution of clouds with varying initial boundary layer stability in Figure 5.4, the cloud development overall is similar for all of the simulations. The small spread which does occur between the results is due to the difference in the time of cloud development. SIM302 and SIM303 produce cloud at a slightly earlier time than the control simulation. SIM303 produces cloud at 1430UTC, one hour before SIM299. The total and maximum cloud fraction is only affected by the stability when the clouds are developing, with a slightly higher fraction in SIM302 and SIM303. The cloud-tops for SIM302 and SIM303 are higher during the developing stage. When the cloud development is in the mature and the decay stages, there is no trend of boundary layer stability within cloud fraction or cloud-top height. The cloud-base height increases with decreasing initial boundary layer stability, consistent with the increase in boundary layer depth.

Figure 5.5 shows the cloud development for the simulations with varying free tropospheric stability. Unlike those with varying boundary layer stability, all clouds develop at the same time as the control simulation, after 1500UTC. The clouds develop identically until they have reached the layer where stability is varied, from 700m up. Thereafter, the clouds in FTM3 develop at a faster rate than the others, reaching maturity at approximately 1730UTC, in comparison to 2000UTC and later for the control simulation and FTP2. The most significant difference between the stabilities is the total cloud fraction and cloud-top height. When cloud development is mature, the total cloud fraction of the FTM3 is almost 10% higher than that of the control simulation. In comparison, the total cloud fraction of FTP2 has reduced by 5% than that of the control simulation. Maximum cloud fraction at a given level also increases with decreased initial free tropospheric stability. The cloud-base height is the same in the simulations initially, but when mature the cloud-base of FTM3 rises more than the other simulations. The cloud-top heights have significant spread. The cloud-top height of FTM3 reaches a maximum of approximately 3.5km, while FTP2 has a lower cloud-top height than the control simulation, of around 2.2km. Although the FTM3 has a cloud depth comparable to that of SIM85 from Section 4 as shown in Figure 4.3, any precipitation was found to be negligible.

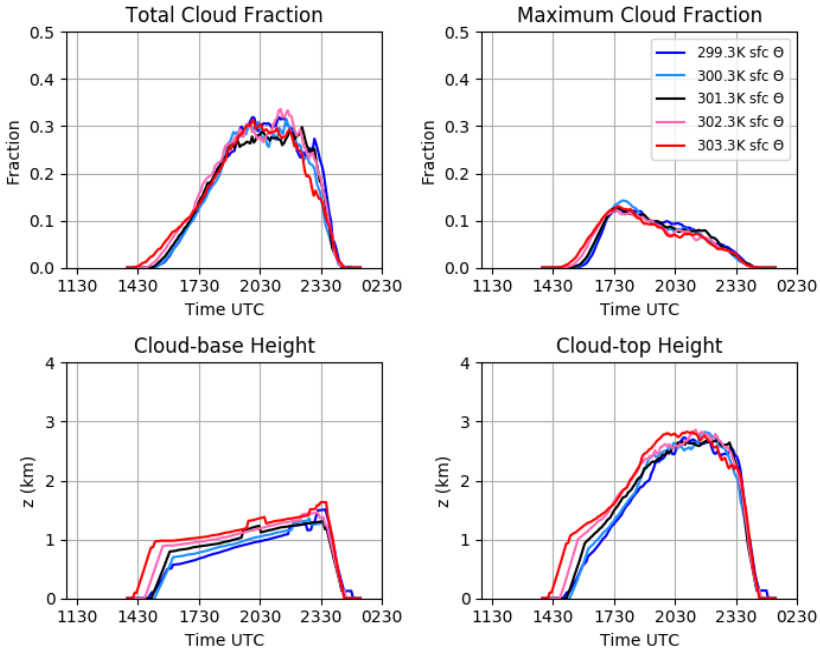

Figure 5.4: The general evolution of clouds between the simulations with varying initial boundary layer potential temperature profiles. Navy, blue, black, pink and red lines correspond to SIM299, SIM300, SIM301, SIM302, and SIM303 respectively.

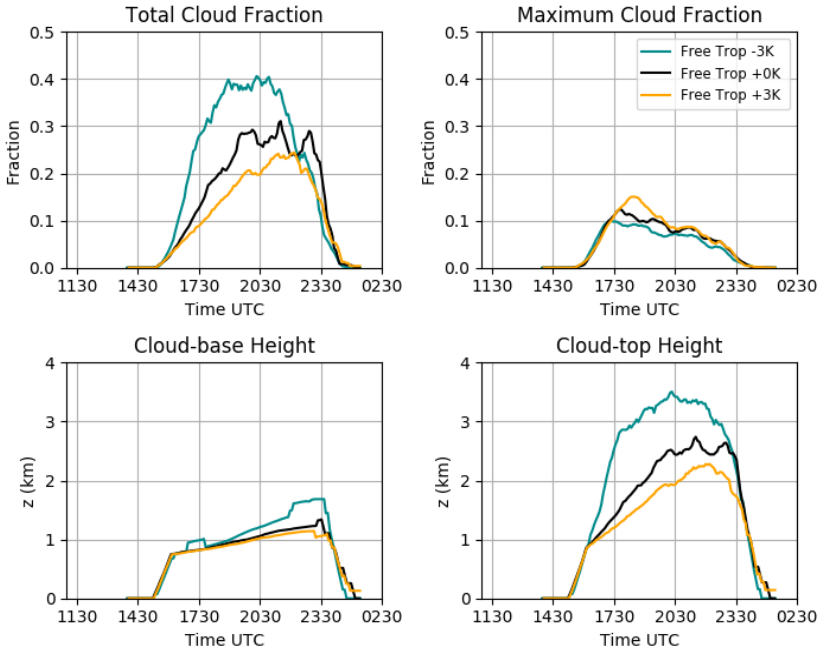

Figure 5.5: The evolution of clouds between the simulations with varying initial free troposphere potential temperature profiles. Green, black and yellow lines correspond to FTM3, the control simulation and FTP2 respectively.

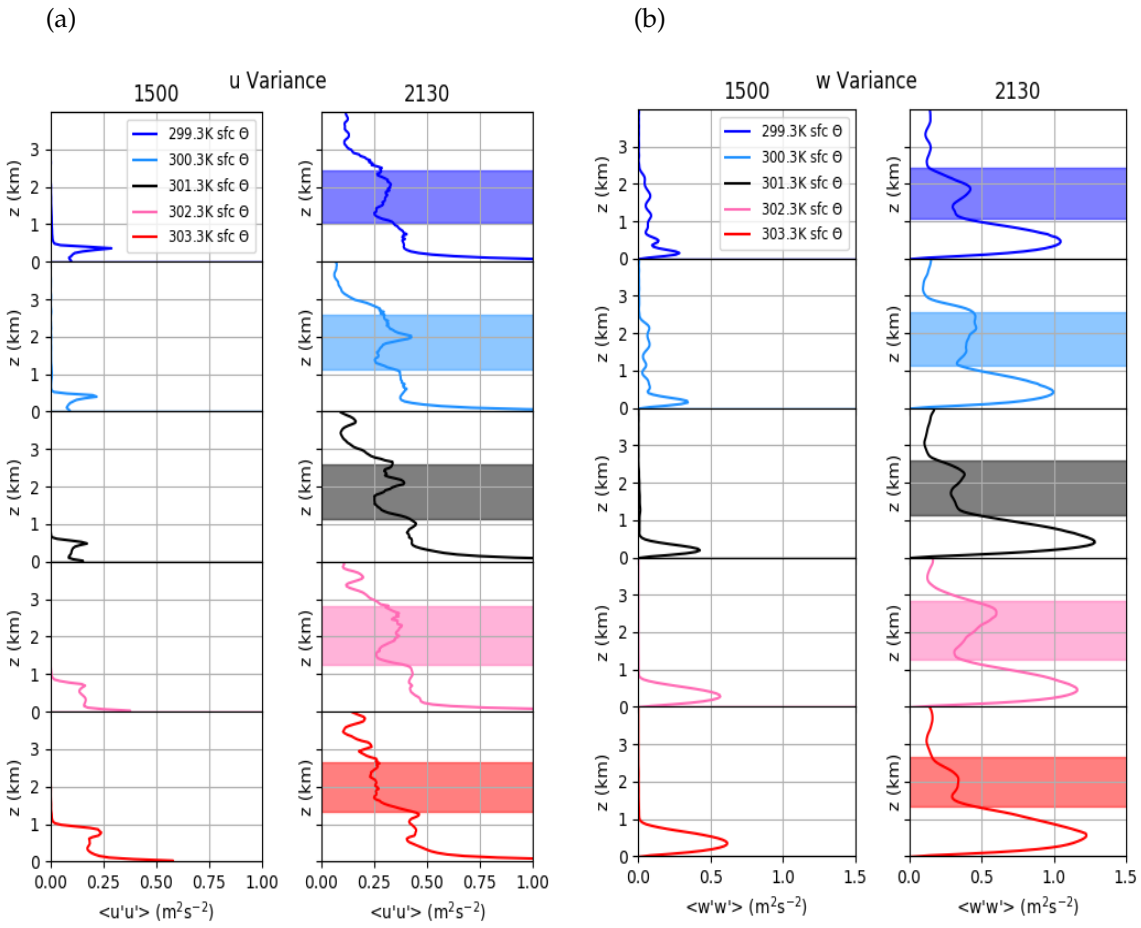

Figure 5.6: The (a) horizontal and (b) vertical velocity variance at two times, 1500UTC and 2130UTC. Navy, blue, black, pink and red lines correspond to SIM299, SIM300, SIM301, SIM302, and SIM303 respectively. Shaded regions correspond to the depth of the cloud layer at that time.

5.4 Velocity Variance

Figure 5.6 shows the comparison of horizontal and vertical velocity variance at two different times, for the simulations with varying initial boundary layer conditions. The times chosen were 1500UTC and 2130UTC, before and after cloud formed in all the simulations. At 1500UTC, the increase of boundary layer depth with increasing initial boundary layer temperature is seen in Figure 5.6a. At this time, SIM299 has a peak of $<u'u'>$ at just over 400m, while in SIM303 the peak occurs at just under 1km. At 2130UTC after cloud has formed, all simulations behave similarly to the control simulation, with an increase in the magnitude of $<u'u'>$ throughout the depth of the cloud layer. The magnitude of $<u'u'>$ in the subcloud layer increases slightly in SIM302 and SIM303, but in general there is no significant change in $<u'u'>$ at 2130UTC between the simulations. Figure 5.6b shows the comparison of $<w'w'>$ between the simulations. Before clouds form at 1500UTC, the magnitude of the $<w'w'>$ peak in the boundary layer clearly increases in SIM302 and SIM303. However, after clouds have formed at 2130UTC,

all simulations have the same structure as found in the control simulation, and no trends can be seen by varying the initial stability.

The same analysis is given to the horizontal and vertical variance for the simulations with varying tropospheric stability, shown in Figure 5.7. Before the formation of clouds at 1530UTC, both the $< u'u' >$ and $< w'w' >$ behave identically in the three simulations. After cloud has formed at 2130UTC, the magnitudes of $<u'u'>$ and $<w'w'>$ within the cloud layer increase in FTM3, and decrease in FTP2, in comparison to the control simulation.

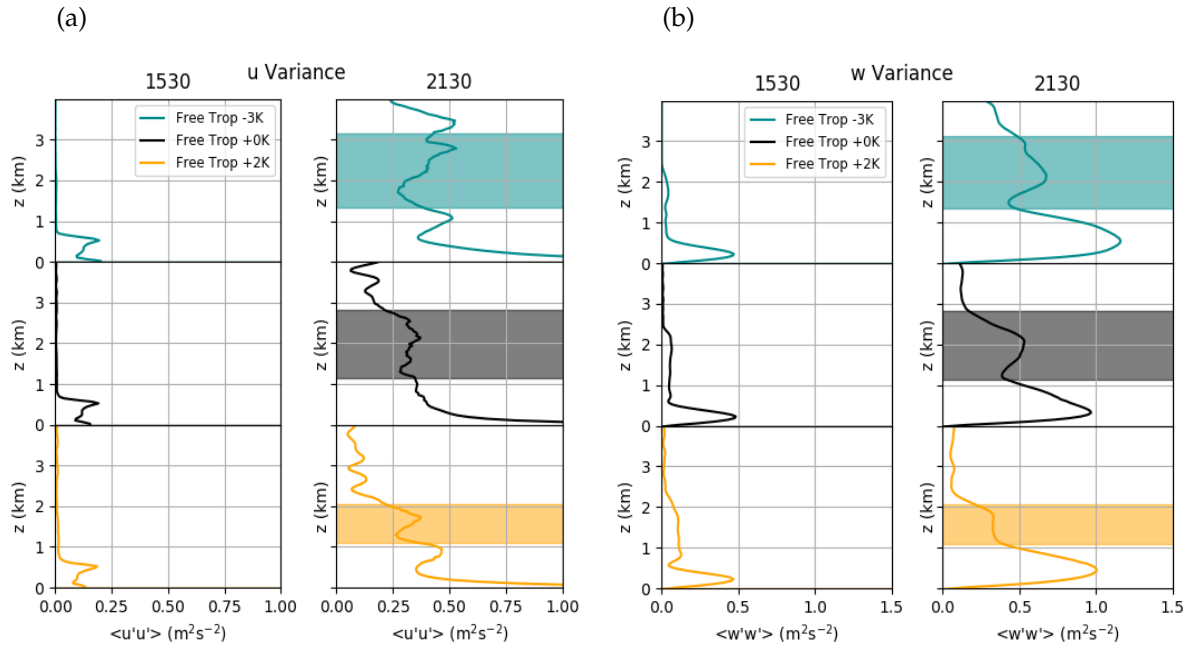

Figure 5.7: The (a) horizontal and (b) vertical velocity variance at two times, 1500UTC and 2130UTC. Green, black and yellow lines correspond to FTM3, the control simulation and FTP2 respectively. Shaded regions correspond to the depth of the cloud layer at that time.

5.5 Core Fraction and Mass Flux

The core fraction and core mass flux are examined during a time of rapid cloud development, and at a later time when clouds are mature. The results from varying initial boundary layer stability (not shown) are not found to affect the core fraction or mass flux, and the results are similar to that found in the control simulation, described in Section 3.5. The initial free tropospheric stability however is found to impact the core fraction. Figure 5.8 shows the profiles of core fraction and core mass flux at 1800UTC and 2100UTC. At 1800UTC in Figure 5.8a, the core fraction throughout the cloud layer has increased in FTM3 in comparison to the control simulation. FTP2 has a much lower core fraction within a shallower cloud layer than that of the control simulation. As seen previously, core fraction peaks near the cloud-base when quickly developing and when clouds are in their mature stage core fraction increases throughout the

entire cloud layer. This structure again holds for core mass flux in Figure 5.8b. This graph clearly shows the increase of core mass flux with a reduction of initial free tropospheric stability. FTM3 has approximately one and a half times the mass flux of FTP2 when the clouds are rapidly developing.

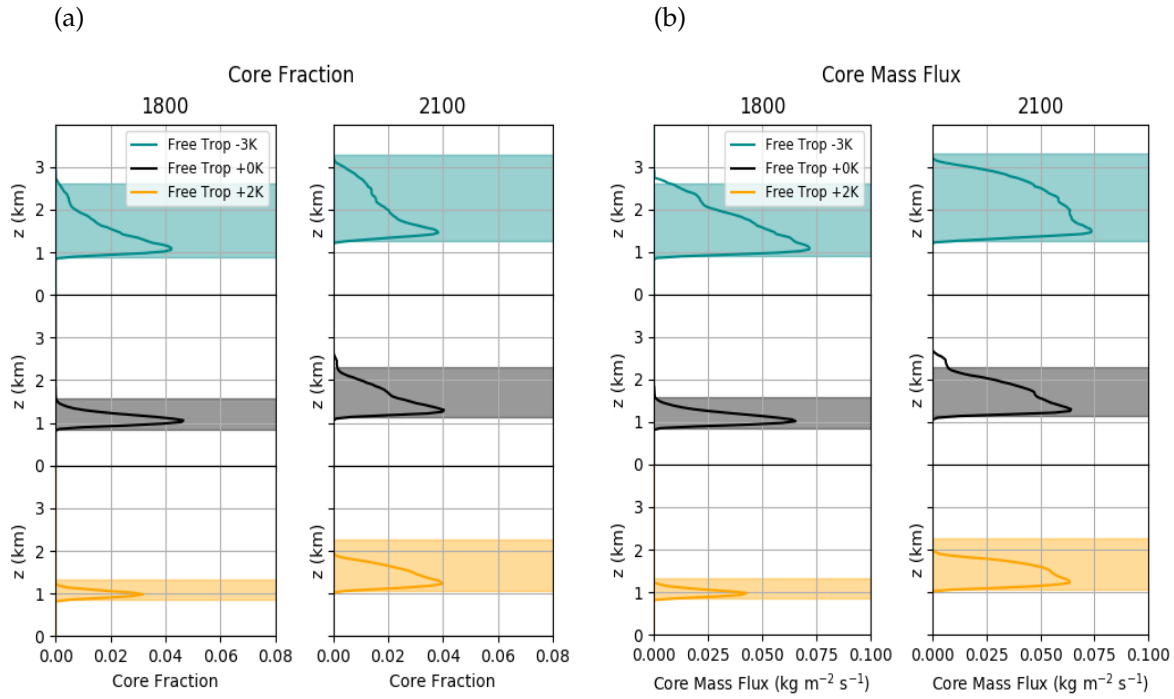

Figure 5.8: (a) Core fraction and (b) core mass flux at two times, 1800UTC and 2100UTC. Green, black and yellow lines correspond to FTM3, the control simulation and FTP2 respectively. Shaded regions mark cloud depth at that time.

5.6 Discussion

Shallow convection is found to be impacted by a change of initial atmospheric stability. However, the impact varies depending on the location of the stability changes within the atmosphere. In general, stability changes of the boundary layer impact boundary layer convection, and the early development of boundary layer cloud. Free tropospheric stability influences the advancement of boundary layer cloud and the strength of moist convection in the free troposphere.

A warming or cooling of the initial boundary layer affects shallow convection during the early stages of the diurnal cycle. A reduction of boundary layer stability is seen to increase dry boundary layer convection. This enhances mixing in the boundary layer which deepens it and produces more uniform profiles of potential temperature and moisture in the boundary layer throughout the simulation. The strengthening of convection in a more initially unstable boundary layer expedites the formation of boundary layer cloud, in comparison to initially

more stable boundary layers. However, when clouds grow to maturity and higher into the atmosphere, the boundary layer stability no longer has any impact on the development and all of the clouds behave in a similar manner. The trend of increasing velocity variance with less stable profiles is further evidence of the strengthened convection within the boundary layer. This trend is no longer seen after clouds have matured. The initial boundary layer stability does not influence the shallow convection in the later hours of the diurnal cycle.

In contrast, the early stages of the diurnal cycle are not affected by varying initial free tropospheric stability. Unsurprisingly, the stability of the free troposphere impacts the cloud development after clouds form and the convection has advanced beyond the boundary layer. The moist shallow convection deepens and cloud cover is amplified for a less stable free troposphere. These results are in agreement with that found by Chlond et al. (2014), who concluded that for a given soil moisture, a less stably stratified atmosphere produces higher mean cloud cover than one that is more stable. Cloud-top heights increase by almost 1km for a 3K reduction in free troposphere potential temperature. The vertical motion is increased and there is a significant increase in buoyancy. These results are consistent with the sensitivity test discussed in the paper by Brown et al. (2002). They initialised a simulation with an initial potential temperature profile that is 1.7 Kkm^{-1} less stable in the free troposphere than the control simulation. Their results showed an identical evolution as the control simulation until 1800UTC, where thereafter convection reached the less stable layer and clouds grew more rapidly to produce a higher cloud-top than in the control simulation. The results from this dissertation are in agreement with this sensitivity test done by Brown et al. (2002).

Although both stability regimes have an impact on convection, it is clear that it is the stability of the free troposphere that has a significant impact. A 3K difference in potential temperature at 2.5km will produce 10% more cloud than a difference of 3K at the surface. The velocity variance in the cloud layer is also higher for a decrease in free tropospheric stability, than the same reduction of stability in the boundary layer. The cloud depth extends deeper by almost 1km, and will be more buoyant throughout the entire layer, as opposed to just the cloud-base.

6 The Impact of Initial Variability

This section analyses the impact that thermodynamic variability generated internally via decaying convection from the previous cycle has on the development of subsequent shallow convection. The simulations are extended to run for a second consecutive diurnal cycle. For each cycle the large scale forcing is prescribed to balance the imposed surface forcing. Thus, the domain-mean values for potential temperature and mass mixing ratio are the same at the beginning (1130UTC) of each diurnal cycle. There are however horizontal fluctuations in these variables at the beginning of the second cycle. A comparison of this diurnal cycle is made against a simulation in which these fluctuations have been relaxed to the domain-mean at the beginning of the second cycle.

6.1 Inclusion of Initial Variability

In the control simulation, initial potential temperature and mass mixing ratio values are horizontally homogeneous. To investigate the impact of variability on the development and evolution of shallow convection, a simulation is run that initially includes horizontal heterogeneities of initial temperature and humidity. Initial fluctuations in temperature and moisture in the domain are generated from convective activity of a prior cycle. At the beginning of a second diurnal cycle, the initial temperature and moisture fields may have increased variability resulting from the previous diurnal cycle. To produce these the simulation run time is extended to 172800s, to run for two consecutive 24 hour cycles.

It is required that the horizontal mean values for potential temperature and mass mixing ratio at the beginning of the two consecutive cycles are similar. This is to ensure that the model sensitivity of initial heterogeneities in the temperature and humidity fields is being tested, and not the sensitivity to the domain-mean initial conditions. Overnight, an additional large scale forcing is prescribed to maintain the simulation closed in terms of moist static energy over a complete 24 hours period. This energy balance in the entire diurnal cycle allows the domain-mean thermodynamic conditions at the beginning of the second day to be very close to those at the beginning of the first cycle. The first cycle of the simulation is referred to as DAY1, and the second cycle is referred to as DAY2. The cycles DAY1 and DAY2 are initialised with the same

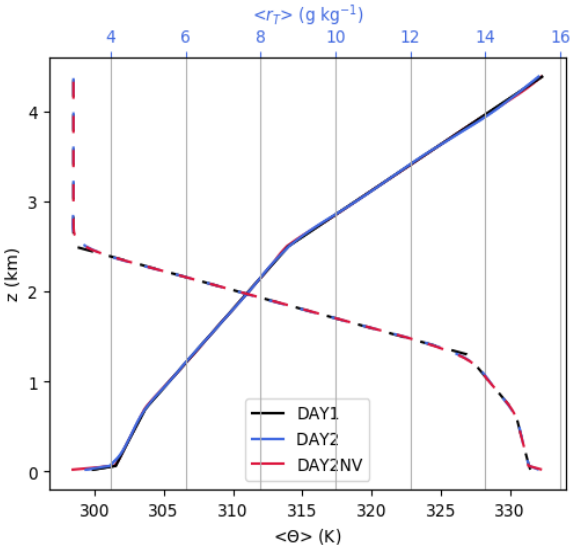

Figure 6.1: Vertical profiles of initial $<\theta>$ (solid line) and $<r_T>$ (dashed line). The black, blue and red lines correspond to the initial profiles in DAY1, DAY2 and DAY2NV, respectively.

domain-mean potential temperature and mass mixing ratio profiles. DAY2 however is initialised with horizontal variability in potential temperature and mixing ratio, that results from the previous cycle. In order to understand whether this variability at the beginning of DAY2 has an impact on the subsequent development of convection, the extended control simulation is repeated to again simulate two consecutive 24 hour cycles. Variability is removed in this simulation from hour 15 to hour 24 (0230UTC to 1130UTC) of the first cycle by relaxing θ and r_T at each gridpoint to the layer mean. The second cycle of this simulation with the removal of variability at the beginning is referred to as DAY2NV. Thus in contrast to DAY2 which is initialised with thermodynamic variability resulting from DAY1, the simulation DAY2NV is initialised with horizontally homogeneous thermodynamic conditions. The evolution of convection in DAY2NV following the removal of horizontal variability is compared to that in DAY2. Figure 6.1 shows the domain-mean initial profiles of potential temperature and total mass mixing ratio for DAY1, DAY2 and DAY2NV. It is clear from Figure 6.1 that all of the initial domain-mean conditions are very close.

6.2 Evolution of Mean Potential Temperature and Mixing Ratio

The evolution of domain-mean thermodynamic profiles in DAY1, DAY2 and DAY2NV are shown in Figure 6.2. The profiles are identical at 1130UTC in all the cycles. There is very little change in the behaviour between DAY1 and DAY2. DAY2NV evolves almost identically in both $<\theta>$ and $<r_T>$ as DAY2. The removal of variability does not change the evolution of the mean profiles on the second diurnal cycle.

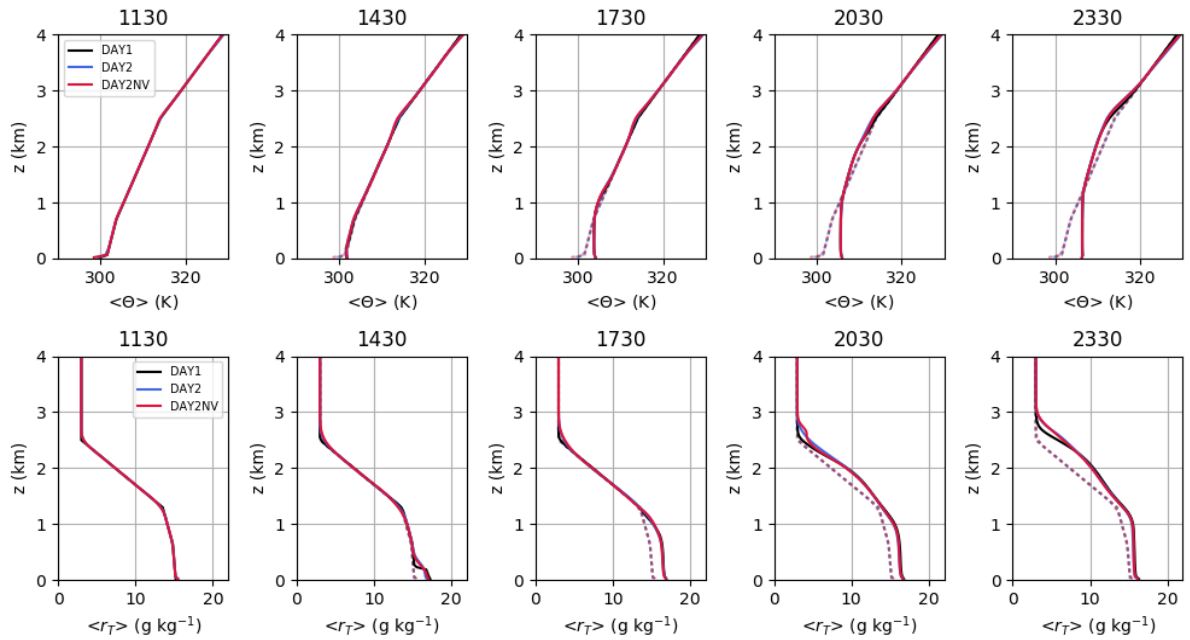

Figure 6.2: Domain-mean potential temperature and mass mixing ratio profiles in DAY1 (black line), DAY2 (blue line) and in the simulation in which initial horizontal variability removed, DAY2NV (red line). Results shown at five different times. Dashed lines represent the initial profiles used during simulations.

6.3 General Cloud Development

Figure 6.3 compares the time series of total cloud fraction, maximum cloud fraction and cloud-base and cloud-top heights between the simulations. In DAY2, there is a small amount of cloud produced in the early morning. This cloud is on or near the surface, and starts to rise from 1300UTC onwards. Thereafter, the cloud evolves in the same manner as DAY1, although the rapid developing stage starts one hour earlier. The development of clouds during the mature and the decay stages are very similar despite the fact that cloud fraction peaks earlier than that in DAY1. The depth and height of the clouds in DAY2 is is also similar to DAY1. After this initial condensation, there is no difference in the amount of cloud produced between DAY1 and DAY2. The peaks of total and maximum cloud fraction are similar. The depth and height of the clouds on DAY2 is also similar to DAY1.

The removal of thermodynamic variability leads to some small changes in cloud development. In DAY2NV, the initial production of cloud near the surface does not occur. The production of boundary layer cloud is delayed in DAY2NV in comparison to DAY2, although clouds still develop earlier than that in DAY1, from approximately 1430UTC onwards. Perhaps the most striking impact of variability on cloud development can be seen in the time series of surface precipitation, shown in Figure 6.4. The DAY2NV produces a relatively significant

amount of rainfall before 2030UTC. DAY1 and DAY2 in comparison produce very little rainfall throughout the cycle.

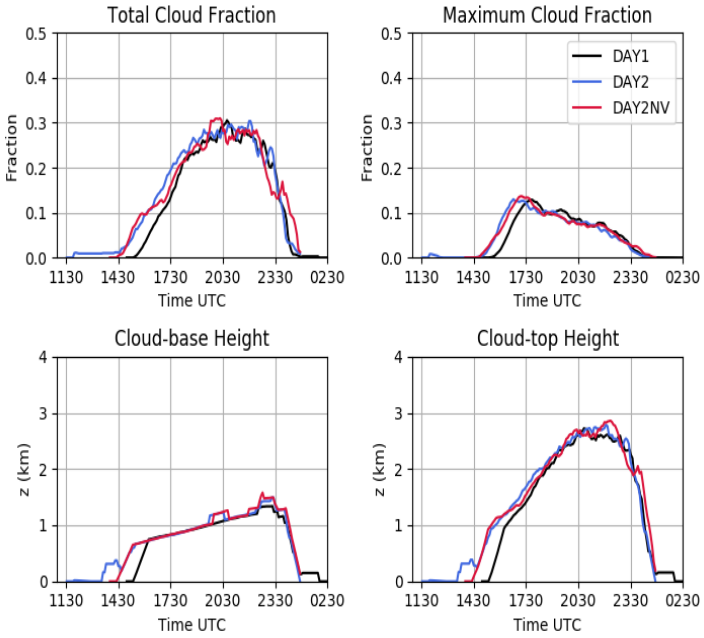

Figure 6.3: Evolution of clouds in DAY1 (black line), DAY2 (blue line) and in the simulation in which initial horizontal variability is removed, DAY2NV (red line).

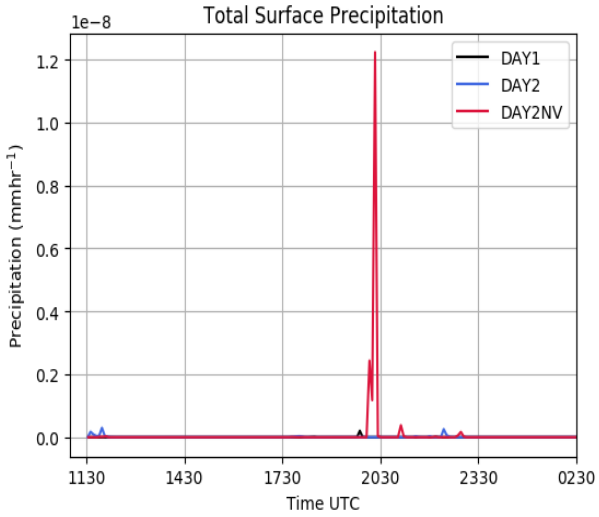

Figure 6.4: Surface precipitation between a simulation in DAY1 (black line), DAY2 (blue line) and in the simulation in which initial horizontal variability is removed, DAY2NV (red line).

6.4 Velocity Variance

The horizontal and vertical velocity variance at two times throughout the simulations is shown in Figure 6.5. As before, the variance before and after cloud development should be compared. However, at an early time when no cloud has formed in all three cycles, the variance in DAY1 is very low or zero. The times 1530UTC and 2030UTC are therefore chosen so that variance is non-zero in DAY1, DAY2 and DAY2NV, although some cloud had already formed in DAY2 and DAY2NV.

It is clear that at this earlier time there is a significant difference in the variance between DAY1 and DAY2. In DAY2, both the horizontal and vertical variance above the boundary layer have magnitudes of greater than $1\text{m}^2\text{s}^{-2}$. The profiles and magnitude of the variance within the boundary layer are somewhat comparable to DAY1, but the values in the free troposphere at levels of approximately 3km are much higher. This suggests that there is more active motion occurring in the troposphere in DAY2 than in DAY1 at this time. An example of the variance at an earlier time of 1430UTC when no cloud has formed in any of the cycles is included in Appendix A.2. This shows that variance is still significantly stronger on DAY2 than on DAY1 in the absence of cloud, suggesting that the presence of near surface clouds generated in DAY2 is not inducing the variance observed in the free troposphere. At the later time of 2030UTC, the structure of both the horizontal and vertical variance in DAY2 is more similar to that in DAY1, although magnitudes are still higher. The peak of $<w'w'>$ in the cloud layer of DAY2 is over twice that from DAY1 at this time.

The removal of the variability at the beginning of the second cycle is seen to have an impact on the variance throughout the day time. For example, at 1530UTC the magnitudes of both $<u'u'>$ and $<w'w'>$ have been reduced in the free troposphere in DAY2NV in comparison to DAY2, although they are still higher than the values in DAY1 at this time. The magnitudes are also reduced at the time of 2030UTC. In particular the cloud layer peak of $<w'w'>$ is reduced from $1.1\text{m}^2\text{s}^{-2}$ to $0.5\text{m}^2\text{s}^{-2}$, and the variance profiles in DAY2NV are very similar to those in DAY1.

6.5 Core Fraction and Mass Flux

Figure 6.6 shows the fraction of core points and the mass flux of core points between the simulations during the rapid development stage at 1830UTC and during the mature stage at 2030UTC. There is a slight reduction in both core fraction and core mass flux in DAY2 compared to DAY1 during both stages. On DAY1 at both times, core fraction is over 40%, while on DAY2 core fraction is less than 40%. Core fraction and mass flux in DAY2NV is slightly higher than that in Day2 at both times, and are more similar to those in DAY1. This increase in core fraction and mass flux with the removal of initial variability is minimal.

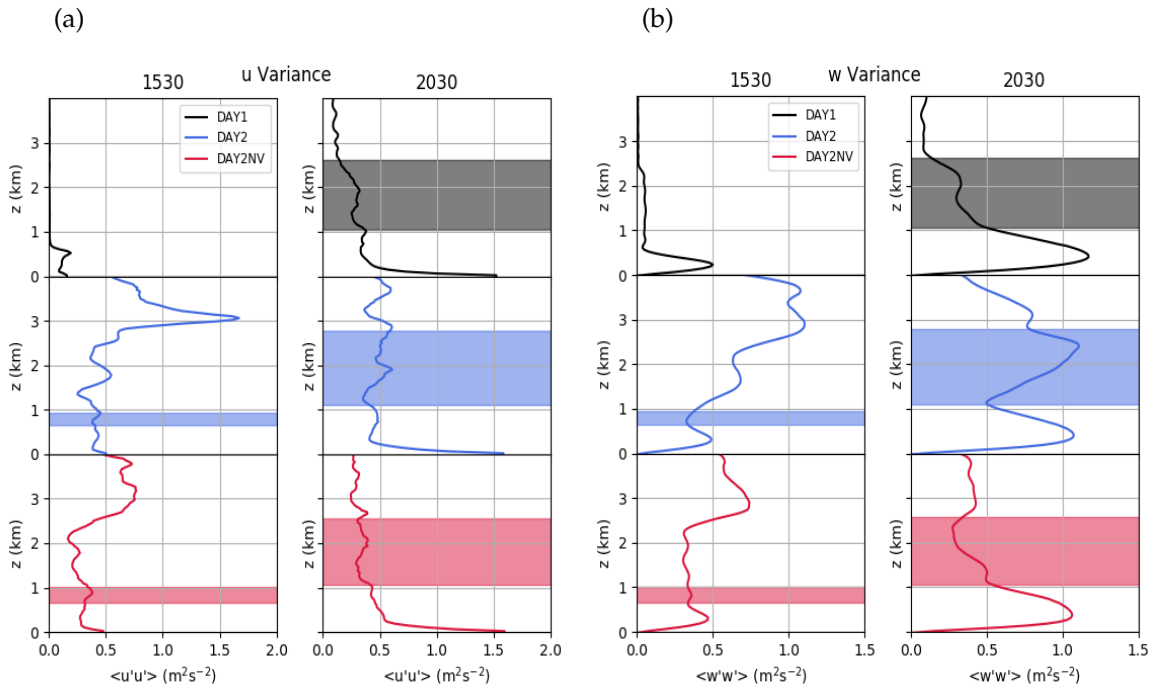

Figure 6.5: The (a) horizontal and (b) vertical velocity variance at two times, 1530UTC and 2030UTC. Black, blue and red lines refer to DAY1, DAY2 and DAY2NV, respectively. Shaded regions correspond to the depth of the cloud layer at that time.

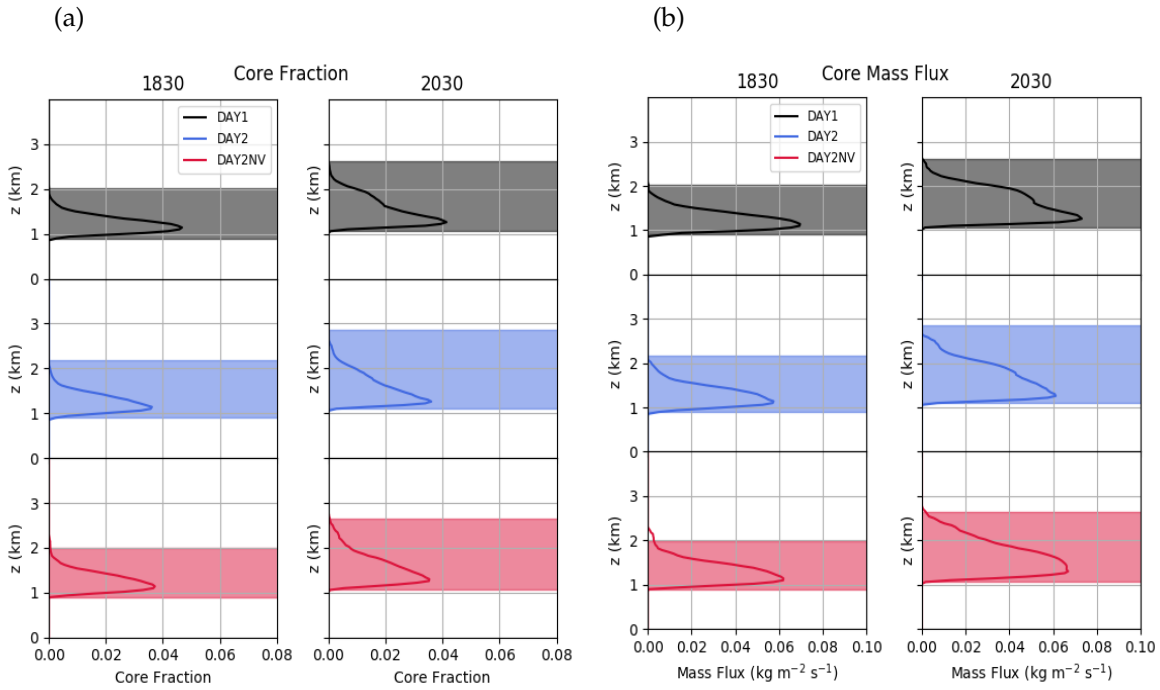

Figure 6.6: (a) Core fraction and (b) core mass flux at two times, 1830UTC and 2030UTC.Black, blue and red lines refer to DAY1, DAY2 and DAY2NV, respectively. Shaded regions correspond to the depth of the cloud layer at that time.

6.6 Discussion

In general, initial horizontal thermodynamic variability has a weaker impact on the evolution of cloud than varying the domain-mean thermodynamic conditions themselves. Horizontal inhomogeneous thermodynamic conditions leads to early development of cloud. The production of cloud occurs near the surface, shortly after the beginning of surface forcing. These near surface clouds formed in the presence of variability as fluctuations of temperature or humidity in the domain may result in saturated regions. Despite having this near surface cloud, the rapid development of clouds growing from the surface into the boundary layer and free troposphere is observed at 1430UTC, one hour earlier than the first diurnal cycle. This is in agreement with the conclusions of Petch et al. (2002), who found that convection occurred 1 to 3 hours earlier with initial spatial thermodynamic variability included. The variability of potential temperature and mixing ratio is shown to have little impact on cloud fraction and mass flux. However, variability has a significant impact on the velocity variance. For example, horizontal and vertical mixing is increased in the simulation that includes variability at the start of surface forcing. However it was not possible to link the early formation of near surface cloud to the horizontal and vertical mixing at upper levels. The increase in velocity variance when initial variability is present may be a result of initial fluctuations of temperature and moisture in the domain driving circulations or eddies that enhance mixing and turbulence. During the mature stage, the velocity variances in DAY1 and DAY2 are similar, indicating that the effects of the initial thermodynamic fluctuations have decayed by this time.

Another notable influence of variability is on precipitation processes. The removable of variability causes a production of precipitation in the afternoon. This result is surprising as it is in contradiction with that from literature, which concluded that initial variability significantly increases the precipitation amount (Stirling and Petch, 2004). Precipitation is produced when initial variability is removed but the peak rainfall is still less than 10% of that found by increasing the initial humidity condition, as discussed in Section 4, shown in Figure 4.5. This study focuses on the analysis of the simulation of the diurnal cycle of shallow convection, with less interest on the production of precipitation. For that reason, the comparison of the results of this study with those of Stirling and Petch (2004) should be done with caution, as they investigate the impact of thermodynamic fluctuations on the diurnal cycle of deep precipitating convection.

7 Conclusion

MONC is used to preform the same simulation of a diurnal cycle of summertime shallow convection as in Brown et al. (2002). The results from MONC are within the results of the ensemble of CRMs given in Brown et al. (2002). Thus, MONC can suitably simulate the diurnal cycle of shallow convection over land. Since MONC can accurately simulate the various processes associated with shallow convection, including clear boundary layer convection in the morning, the initial condensation of cloud, and the moist updrafts during the mature stage of cloud development, the further step was taken to investigate the factors that control the development of shallow convection.

It is found that initial atmospheric moisture content has a significant impact on the development of shallow convective clouds. An initially moister environment increases the rate of cloud development, the amount of cloud produced and results in the deepening of convection and cloud layer depth. Vertical ascent is strengthened and cloud-top heights extend higher into the troposphere with increasing initial humidity, as a result of the increase in the moisture transport into the free troposphere. In contrast, an initially drier atmosphere will delay the initiation of clouds, reduce cloud amount and cloud layer depth. In addition, vertical transport of mass and moisture into the free troposphere is reduced.

The initial potential temperature profile of the atmosphere is also found to have an impact on shallow convection. In particular, the stability of the free troposphere can greatly influence the development of clouds. The impact of reducing the stability of the free troposphere on cloud-height and fraction is similar to that of increasing initial humidity. Clouds extend higher and cloud fractions increase due to an initially more unstable free troposphere. Convection is deepened, as transport of moisture from the boundary layer is enhanced. The initiation of clouds is not influenced by free tropospheric stability, and is instead dependent on the stability of the boundary layer. The increase in the rate of cloud development by a reduction of boundary layer stability, is not as large as the increase obtained from increasing initial humidity conditions, with the latter advancing or delaying the initiation of clouds by several hours. Boundary layer stability influences the cloud development during their development stage, but has no impact on shallow convection during the mature or decay stages. A reduction of boundary layer stability acts to enhance convection within the boundary layer, but has little effect on that in the free troposphere. The reverse is true for the stability of the free troposphere. Other

than the impact on the initiation of clouds, the initial free tropospheric stability and initial humidity have comparable effects on the development of clouds. Increasing initial humidity and reducing free tropospheric stability both deepen shallow convection and strengthen vertical motion and transport into the free troposphere.

The effect of initial thermodynamic variability on subsequent development of shallow convection is found to be much weaker than that of varying the domain-mean thermodynamic initial conditions. The presence of variability of potential temperature and humidity causes the initiation of clouds to occur one hour earlier. The impact of the initial variability on the time of cloud production is less influential than that from varying the initial humidity conditions. Initial variability is found to increase vertical and horizontal mixing, particularly in the free troposphere. This influence of variability on velocity variance is stronger than that seen from varying the initial domain-mean conditions. Initial thermodynamic variability is seen to have no impact on the amount of cloud, or cloud depths during the mature and decay stages of development.

MONC can accurately simulate the diurnal cycle of shallow convection over land. The diurnal cycle of shallow convection is controlled chiefly by the domain-mean initial thermodynamic conditions, whilst the initial horizontal variations in the thermodynamic fields have a weaker impact. The initial humidity profile of the atmosphere has the largest impact on the development of shallow clouds. The initial stability of the free troposphere is also found to have a major influence on cloud development, whilst the stability of boundary layer has a weaker impact. The weakest impact on shallow convection is found to be due to the presence of initial fluctuations of temperature and humidity in the atmosphere.

It is clear therefore that these sensitivities should be considered when modelling shallow convection. These simulations are somewhat simplified and do not however take into account certain aspects of shallow convection such as spatial variability of initial conditions. A possible extension of this work could be to investigate the influence surface fluxes would have on the development of shallow convection, if they were not horizontally, uniformly imposed across the domain. Another extension of this work could be to explore a more complex combination of initial atmospheric conditions. The combined effects that initial humidity and stability have on the evolution of shallow convection could be explored by running simulations that vary the initial humidity and potential temperature profiles simultaneously.

A Appendix

A.1 Model Set Up

A.1.1 Large Scale Forcings

The large scale forcings including advective tendency (A_θ), radiative tendency (R_θ) and advective mean total mass mixing ratio (A_{r_T}) are shown in Figure A.1.

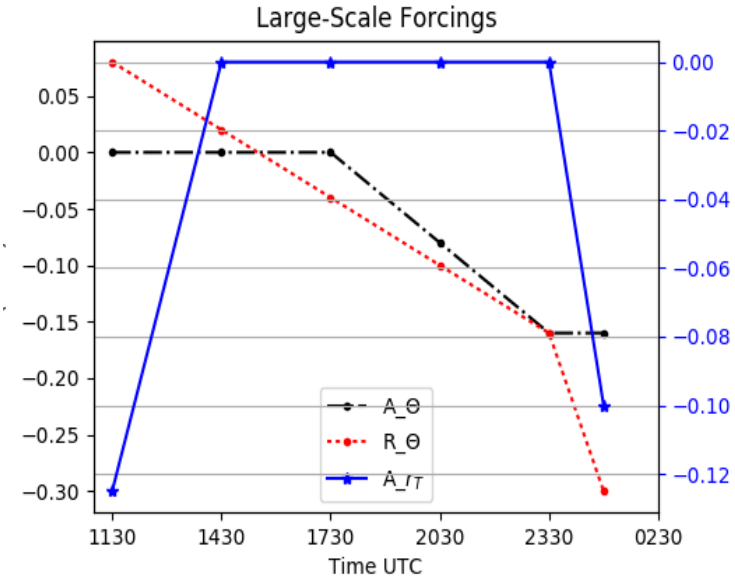

Figure A.1: Time series of the large scale forcings prescribed throughout all the simulations. Values applied as described in Section 3.

A.1.2 Surface Forcings

The values of the imposed surface forcings used in the control simulation are shown in Table A.1.

Hour (UTC)	SHF (Wm^{-2})	LHF (Wm^{-2})
1130	-30	5
1530	90	250
1800	140	450
1900	140	500
2130	100	420
0000	-10	180
0200	-10	0

Table A.1: Fluxes for the sensible heat (SHF) and latent heat (LHF) imposed in the control simulation, as used by Brown et al. (2002). Fluxes during intermediate times were determined using linear interpolation.

A.1.3 Initial Profiles

The domain-mean values for the initial profiles of θ and r_T used in the control simulation are shown in Table A.2

z (km)	$<\theta>$ (K)	$<r_T>$ (g kg^{-1})
0.0	299.00	15.20
50.0	301.50	15.17
350.0	302.50	14.98
650.0	303.53	14.80
700.0	303.70	14.70
1300.0	307.13	13.50
2500.0	314.00	3.00
5500.0	343.20	3.00

Table A.2: Values for the initial domain-mean potential temperature and mass mixing ratio imposed in the control simulation, as used by Brown et al. (2002). Values on intermediate levels were determined using linear interpolation.

A.2 Variability

Figure A.2 shows the velocity variance in the simulation at an earlier time of 1430UTC and 2030UTC. At 1430UTC, the variance is negligible in DAY1. However in DAY2, the variance is quite high, particularly in the free troposphere.

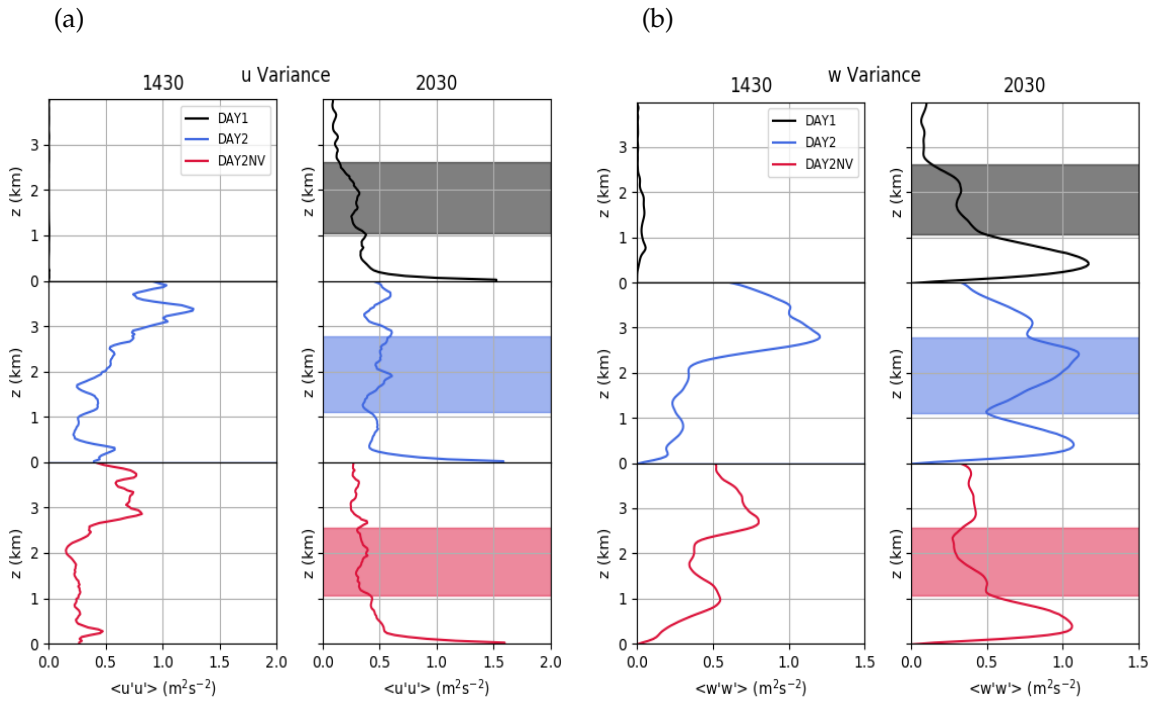

Figure A.2: The (a) horizontal and (b) vertical velocity variance at two times, 1430UTC and 2030UTC. Black, blue and red lines refer to DAY1, DAY2 and DAY2NV, respectively. Shaded regions correspond to depth of cloud layer at that time.

B Bibliography

Arakawa, A., and W. H. Schubert, 1974: Interaction of a Cumulus Cloud Ensemble with the Large-Scale Environment, Part I. *Journal of the Atmospheric Sciences*, **31 (3)**, 674–701, doi:10.1175/1520-0469(1974)031<0674:IOACCE>2.0.CO;2.

Bechtold, P., J.-P. Chaboureau, A. Beljaars, A. K. Betts, M. Köhler, M. Miller, and J.-L. Redelsperger, 2004: The simulation of the diurnal cycle of convective precipitation over land in a global model. *Quarterly Journal of the Royal Meteorological Society*, **130 (604)**, 3119–3137, doi:https://doi.org/10.1256/qj.03.103.

Bechtold, P., I. Sandu, D. Klocke, N. Semane, M. Ahlgrimm, A. Beljaars, R. Forbes, and M. Rodwell, 2014: The role of shallow convection in ECMWF's Integrated Forecasting System. **(725)**, 27, doi:10.21957/heba1qwem.

Boutle, I. A., S. E. Belcher, and R. S. Plant, 2011: Moisture transport in midlatitude cyclones. *Quarterly Journal of the Royal Meteorological Society*, **137 (655)**, 360–373, doi:10.1002/qj.783.

Brown, A. R., and Coauthors, 2002: Large-eddy simulation of the diurnal cycle of shallow cumulus convection over land. *Quarterly Journal of the Royal Meteorological Society*, **128 (582)**, 1075–1093, doi:10.1256/003590002320373210.

Brown, N., A. Nigay, M. Weiland, A. Hill, and B. Shipway, 2017: Porting the microphysics model CASIM to GPU and KNL Cray machines. *Cray User Group 2017*, WA, United States, 14pp.

Brown, N., M. Weiland, A. Hill, B. Shipway, C. Maynard, T. Allen, and M. Rezny, 2015: A Highly Scalable Met Office NERC Cloud Model. *Proceedings of the 3rd International Conference on Exascale Applications and Software*, University of Edinburgh, Edinburgh, Scotland, UK, 132–137.

Cai, Q., G. J. Zhang, and T. Zhou, 2013: Impacts of Shallow Convection on MJO Simulation: A Moist Static Energy and Moisture Budget Analysis. *Journal of Climate*, **26 (8)**, 2417–2431, doi:10.1175/JCLI-D-12-00127.1.

Chen, C.-A., J.-Y. Yu, and C. Chou, 2016: Impacts of Vertical Structure of Convection in Global Warming: The Role of Shallow Convection. *Journal of Climate*, **29 (12)**, 4665–4684, doi:10.1175/JCLI-D-15-0563.1.

Chlond, A., O. Böhringer, T. Auerswald, and F. Müller, 2014: The effect of soil moisture and atmospheric conditions on the development of shallow cumulus convection: A coupled large-eddy simulation–land surface model study. *Meteorologische Zeitschrift*, **23 (5)**, 491–510.

Chou, C., and C.-A. Chen, 2010: Depth of Convection and the Weakening of Tropical Circulation in Global Warming. *Journal of Climate*, **23 (11)**, 3019–3030, doi:10.1175/2010JCLI3383.1.

Dai, A., F. Giorgi, and K. E. Trenberth, 1999: Observed and model-simulated diurnal cycles of precipitation over the contiguous United States. *Journal of Geophysical Research: Atmospheres*, **104 (D6)**, 6377–6402.

Derbyshire, S. H., I. Beau, P. Bechtold, J.-Y. Grandpeix, J.-M. Piriou, J.-L. Redelsperger, and P. M. M. Soares, 2004: Sensitivity of moist convection to environmental humidity. *Quarterly Journal of the Royal Meteorological Society*, **130 (604)**, 3055–3079, doi:10.1256/qj.03.130.

Edwards, J. M., and A. Slingo, 1996: Studies with a flexible new radiation code. I: Choosing a configuration for a large-scale model. *Quarterly Journal of the Royal Meteorological Society*, **122 (531)**, 689–719, doi:10.1002/qj.49712253107.

Esbensen, S., 1978: Bulk Thermodynamic Effects and Properties of Small Tropical Cumuli. *Journal of the Atmospheric Sciences*, **35 (5)**, 826–837, doi:10.1175/1520-0469(1978)035<0826:BTEAPO>2.0.CO;2.

Fast, J. D., and Coauthors, 2019: Overview of the HI-SCALE Field Campaign: A New Perspective on Shallow Convective Clouds. *Bulletin of the American Meteorological Society*, **100 (5)**, 821–840, doi:10.1175/BAMS-D-18-0030.1.

Frierson, D. M. W., 2007: The Dynamics of Idealized Convection Schemes and Their Effect on the Zonally Averaged Tropical Circulation. *Journal of the Atmospheric Sciences*, **64 (6)**, 1959–1976, doi:10.1175/JAS3935.1.

Gray, M. E. B., J. Petch, S. Derbyshire, A. Brown, A. Lock, H. Swann, and P. Brown, 2001: Version 2.3 of the Met Office Large Eddy Model. *Met Office (APR) Turbulence and Diffusion Rep*, **276**.

Gustafson, W. I., A. M. Vogelmann, X. Cheng, S. Endo, B. Krishna, Z. Li, T. Toto, and H. Xiao, 2017: Recommendations for the Implementation of the LASSO Workflow. Tech. Rep. DOE/SC-ARM-17-031, 42 pp. doi:10.2172/1406259.

Hartmann, D., M. E. Ockert-Bell, and M. L. Michelsen, 1992: The Effect of Cloud Type on Earth's Energy Balance: Global analysis. *Journal of Climate*, **5**, doi:10.1175/1520-0442.

Holloway, C. E., and J. D. Neelin, 2009: Moisture Vertical Structure, Column Water Vapor, and Tropical Deep Convection. *Journal of the Atmospheric Sciences*, **66 (6)**, 1665–1683, doi:10.1175/2008JAS2806.1.

Kain, J. S., and J. M. Fritsch, 1990: A One-Dimensional Entraining/Detraining Plume Model and Its Application in Convective Parameterization. *Journal of the Atmospheric Sciences*, **47 (23)**, 2784–2802, doi:10.1175/1520-0469(1990)047<2784:AODEPM>2.0.CO;2.

Lenderink, G., and Coauthors, 2004: The diurnal cycle of shallow cumulus clouds over land: A single-column model intercomparison study. *Quarterly Journal of the Royal Meteorological Society*, **130 (604)**, 3339–3364, doi:10.1256/qj.03.122.

Neggers, R. A. J., J. D. Neelin, and B. Stevens, 2007: Impact Mechanisms of Shallow Cumulus Convection on Tropical Climate Dynamics. *Journal of Climate*, **20 (11)**, 2623–2642, doi:10.1175/JCLI4079.1.

Petch, J. C., A. R. Brown, and M. E. B. Gray, 2002: The impact of horizontal resolution on the simulations of convective development over land. *Quarterly Journal of the Royal Meteorological Society*, **128 (584)**, 2031–2044, doi:10.1256/003590002320603511.

Plant, R., and J. Yano, 2016: *Parameterization of Atmospheric Convection*, Vol. 2. Imperial College Press, 617 pp., doi:https://doi.org/10.1142/p1005.

Plant, R. S., and G. C. Craig, 2008: A Stochastic Parameterization for Deep Convection Based on Equilibrium Statistics. *Journal of the Atmospheric Sciences*, **65 (1)**, 87–105, doi:10.1175/2007JAS2263.1.

Rieck, M., L. Nuijens, and B. Stevens, 2012: Marine Boundary Layer Cloud Feedbacks in a Constant Relative Humidity Atmosphere. *Journal of Atmospheric Sciences*, **69**, 2538–2550, doi:10.1175/JAS-D-11-0203.1.

Salathé, E. P., and D. L. Hartmann, 1997: A Trajectory Analysis of Tropical Upper-Tropospheric Moisture and Convection. *Journal of Climate*, **10 (10)**, 2533–2547, doi:10.1175/1520-0442(1997)010<2533:ATAOTU>2.0.CO;2.

Siebesma, A. P., 1998: *Shallow Cumulus Convection*, 441–486. Springer Netherlands, Dordrecht, doi:10.1007/978-94-011-5058-3_19.

Siebesma, A. P., and J. W. M. Cuijpers, 1995: Evaluation of Parametric Assumptions for Shallow Cumulus Convection. *Journal of the Atmospheric Sciences*, **52 (6)**, 650–666, doi:10.1175/1520-0469(1995)052<0650:EOPAFS>2.0.CO;2.

Siebesma, A. P., P. M. M. Soares, and J. Teixeira, 2007: A Combined Eddy-Diffusivity Mass-Flux Approach for the Convective Boundary Layer. *Journal of the Atmospheric Sciences*, **64 (4)**, 1230–1248, doi:10.1175/JAS3888.1.

Stevens, B., and Coauthors, 2001: Simulations of Trade Wind Cumuli under a Strong Inversion. *Journal of the Atmospheric Sciences*, **58 (14)**, 1870–1891, doi:10.1175/1520-0469(2001)058<1870:SOTWCU>2.0.CO;2.

Stirling, A. J., and J. C. Petch, 2004: The impacts of spatial variability on the development of convection. *Quarterly Journal of the Royal Meteorological Society*, **130 (604)**, 3189–3206, doi:10.1256/qj.03.137.

Su, H., J. H. Jiang, C. Zhai, T. J. Shen, J. D. Neelin, G. L. Stephens, and Y. L. Yung, 2014: Weakening and strengthening structures in the Hadley Circulation change under global warming and implications for cloud response and climate sensitivity. *Journal of Geophysical Research: Atmospheres*, **119 (10)**, 5787–5805, doi:10.1002/2014JD021642.

Tiedtke, M., 1989: A Comprehensive Mass Flux Scheme for Cumulus Parameterization in Large-Scale Models. *Monthly Weather Review*, **117 (8)**, 1779–1800, doi:10.1175/1520-0493(1989)117<1779:ACMFSF>2.0.CO;2.

Tiedtke, M., W. A. Heckley, and J. Slingo, 1988: Tropical forecasting at ECMWF: The influence of physical parametrization on the mean structure of forecasts and analyses. *Quarterly Journal of the Royal Meteorological Society*, **114 (481)**, 639–664, doi:10.1002/qj.49711448106.

Vecchi, G. A., and B. J. Soden, 2007: Global Warming and the Weakening of the Tropical circulation. *Journal of Climate*, **20 (17)**, 4316–4340, doi:10.1175/JCLI4258.1.

Von Salzen, K., N. A. McFarlane, and M. Lazare, 2005: The role of shallow convection in the water and energy cycles of the atmosphere. *Climate Dynamics*, **25 (7)**, 671–688, doi:10.1007/s00382-005-0051-2.

Williams, K. D., and G. Tselioudis, 2007: GCM intercomparison of global cloud regimes: present-day evaluation and climate change response. *Climate Dynamics*, **29 (2)**, 231–250, doi:10.1007/s00382-007-0232-2.

Wu, C.-M., B. Stevens, and A. Arakawa, 2009: What Controls the Transition from Shallow to Deep Convection? *Journal of the Atmospheric Sciences*, **66 (6)**, 1793–1806, doi:10.1175/2008JAS2945.1.

Xu, K.-M., and Coauthors, 2002: An intercomparison of cloud-resolving models with the atmospheric radiation measurement summer 1997 intensive observation period data. *Quarterly Journal of the Royal Meteorological Society*, **128 (580)**, 593–624, doi:10.1256/003590002321042117.

Zhang, M. H., and Coauthors, 2005: Comparing clouds and their seasonal variations in 10 atmospheric general circulation models with satellite measurements. *J. Geophys. Res.*, **110**, D15S02, doi:10.1029/2004JD005021.

Zhang, Y., and S. A. Klein, 2010: Mechanisms Affecting the Transition from Shallow to Deep Convection over Land: Inferences from Observations of the Diurnal Cycle Collected at the ARM Southern great Plains Site. *Journal of the Atmospheric Sciences*, **67 (9)**, 2943–2959, doi: 10.1175/2010JAS3366.1.